

1           **Transverse energy analysis of**  
2           **relativistic heavy ion collisions**  
3   **through the use of identified particles**  
4           **spectra**

5                   A Thesis Presented for the  
6                   Master of Science  
7                   Degree  
8           The University of Tennessee, Knoxville

9                   Biswas Sharma

10                  May 2018

11

© by Biswas Sharma, 2018

12

All Rights Reserved.

# Abstract

This thesis presents an analysis of the transverse energy resulting from the collisions of gold nuclei at the Relativistic Heavy Ion Collider in Brookhaven National Laboratory. The transverse momentum distributions available from the STAR detector corresponding to nine different centralities for eight different identified particles,  $\pi^\pm$ ,  $K^\pm$ ,  $\Lambda^\pm$ ,  $p$ , and  $\bar{p}$ , resulting from the collisions at five different center-of-mass energies per nucleon – 7.7, 11.5, 19.6, 27, and 39 GeV – are used in the calculations of the corresponding transverse energies. The results, when compared with the calorimetric transverse energy measurement from the PHENIX detector, show some discrepancy.

# Table of Contents

23	<b>1 Introduction</b>	<b>1</b>
24	<b>2 Theoretical Background</b>	<b>3</b>
25	2.1 Quantum Chromodynamics . . . . .	3
26	2.2 Phase Transitions . . . . .	4
27	2.3 Quark-Gluon Plasma . . . . .	5
28	<b>3 Relativistic Heavy Ion Collisions</b>	<b>7</b>
29	3.1 RHIC and LHC . . . . .	7
30	3.2 Collision Energy and Geometry . . . . .	9
31	3.3 QGP Evolution . . . . .	11
32	3.4 Detection of Collision Products . . . . .	12
33	3.5 Detection of QGP Signatures . . . . .	12
34	3.5.1 Bjorken Energy Density . . . . .	13
35	3.5.2 Elliptic Flow . . . . .	14
36	3.5.3 Prompt and Thermal Photons . . . . .	15
37	3.5.4 Strangeness Enhancement . . . . .	16
38	3.5.5 Jet Quenching . . . . .	17
39	3.6 The Beam Energy Scan Program . . . . .	19
40	<b>4 Measurement of Transverse Energy</b>	<b>21</b>
41	4.1 Definition of Transverse Energy . . . . .	21
42	4.2 $E_T$ Measurement with Calorimeters . . . . .	22

43	4.2.1	Calorimeter . . . . .	22
44	4.2.2	$E_T$ from PHENIX Calorimetry . . . . .	23
45	4.3	$E_T$ Measurement with Tracking Detectors . . . . .	24
46	4.3.1	Tracking and Particle Identification . . . . .	24
47	4.3.2	Calculation of $\frac{dE_T}{d\eta}$ from $p_T$ spectra . . . . .	25
48	4.3.3	Tracking Detectors in STAR . . . . .	26
49	<b>5</b>	<b>Data Analysis</b>	<b>28</b>
50	5.1	STAR $p_T$ Spectra . . . . .	28
51	5.1.1	Corrections and Systematic Uncertainties . . . . .	29
52	5.2	Extrapolation of Spectra . . . . .	31
53	5.2.1	Boltzmann-Gibbs Blast Wave . . . . .	31
54	5.2.2	Fitting Spectra to BGBW . . . . .	31
55	5.3	Calculations from the Spectra . . . . .	32
56	5.3.1	Calculation of $\frac{dE_T}{dy}$ , $\frac{dE_T}{d\eta}$ , $\frac{dN_{ch}}{dy}$ , and $\frac{dN_{ch}}{d\eta}$ . . . . .	32
57	5.3.2	Assumptions, Estimation of Total $E_T$ , and Uncertainties . . . . .	33
58	5.3.3	Lambdas Centrality Adjustments and $E_T$ Interpolations . . . . .	34
59	<b>6</b>	<b>Results</b>	<b>35</b>
60	<b>7</b>	<b>Conclusion and Future Work</b>	<b>45</b>
61		<b>Bibliography</b>	<b>47</b>
62		<b>Appendices</b>	<b>54</b>
63	A	Kinematic Variables . . . . .	55
64	B	Results from BGBW Fits . . . . .	57

# 65 **List of Tables**

66	3.1 Colliding species and associated collision energies at RHIC [1]. . . . .	10
67	5.1 Isospin states of different identified particles. . . . .	33

# 68 List of Figures

69	2.1	Schematic of the QCD phase diagram [2]. . . . .	6
70	3.1	Initial layout of the RHIC [3]. . . . .	8
71	3.2	An illustration of a mid-central collision of two nuclei traveling in the z	
72		direction. The X-axis is parallel to the line joining the centers of the two	
73		nuclei at the time of collision [4]. . . . .	11
74	3.3	An illustration of a collision consisting of participants (solid red) and	
75		spectators (open blue) within the colliding nuclei labeled A and B. $t_c$ denotes	
76		the time of maximum overlap of the two nuclei. The apparent narrowing of	
77		the volumes of the nuclei in the z-direction is due to Lorentz contraction [5].	12
78	3.4	Evolution of the QGP represented in a lightcone diagram. $\tau_0$ denotes the	
79		formation time of the QGP. $T_c$ is the critical temperature of the transition	
80		from the QGP to the hadron gas phase. $T_{ch}$ and $T_{fo}$ stand for the temperatures	
81		at, respectively, chemical freeze-out and thermal freeze-out [4]. . . . .	13
82	3.5	Minimum-bias Au+Au ( $\sqrt{s_{NN}} = 200\text{GeV}$ ) elliptic flow spectra for identified	
83		particles: (a) $v_2$ vs $p_T$ and (b) $v_2$ vs $KE_T$ [6]. . . . .	15
84	3.6	Minimum-bias Au+Au ( $\sqrt{s_{NN}} = 200\text{GeV}$ ) elliptic flow spectra for identified	
85		particles: (a) $\frac{v_2}{n_q}$ vs $\frac{p_T}{n_q}$ and (b) $\frac{v_2}{n_q}$ vs $\frac{KE_T}{n_q}$ [6]. . . . .	16
86	3.7	Feynman diagram representing the production of photons from quarks and	
87		gluons. (a) and (b) represent annihilation processes, whereas (c) and (d)	
88		represent Compton processes [7]. . . . .	17

89	3.8	Illustration of jet quenching. Two jets are produced from each of the hard	
90		scatterings occuring at the locations of the solid dots. Jets originating closer	
91		to the initial surface are more probable to propagate outside the medium, as	
92		shown. Jets opposite to them interact with the medium, losing their energy	
93		and resulting in bow front shock waves [8]. . . . .	18
94	3.9	$R_{AA}$ from PHENIX for direct photons [9], $\pi^0$ [10], $\eta$ [11], $\phi$ [12], $p$ [13], $J/\psi$ [14],	
95		$\omega$ [15], $e^\pm$ from heavy flavor decays [16], and $K^\pm$ [13]. This demonstrates that	
96		colored probes (high- $p_T$ final state hadrons) are suppressed while electroweak	
97		probes (direct photons) are not at RHIC. . . . .	19
98	4.1	Energy loss distribution in the STAR TPC for primary and secondary particles	
99		[17]. . . . .	27
100	5.1	Transverse momentum spectra for $\pi^+$ , $\pi^-$ , $K^+$ , $K^-$ , $p$ , and $\bar{p}$ at midrapidity	
101		( $ y  < 0.1$ ) from 39 GeV Au+Au collisions at RHIC. The fitting curves	
102		on the 0-5% central collision spectra for pions, kaons, and protons/anti-	
103		protons represent, respectively, the Bose-Einstein, $m_T$ -exponential, and	
104		double-exponential functions [18]. . . . .	29
105	5.2	Midrapidity efficiency $\times$ acceptance as a function of $p_T$ calculated from STAR	
106		TPC Monte Carlo simulation of reconstructing (a) pions, (b) kaons, and (c)	
107		protons for 0-5% central 7.7 GeV Au+Au collisions. The curves represent	
108		functional fits of the form $y \propto e^{-\frac{1}{x}}$ [18]. . . . .	30
109	5.3	Red curve shows the Boltzmann-Gibbs blast wave functional fit on the	
110		preliminary transverse momentum spectrum for lambda particles identified	
111		by the STAR detector for 19.6 GeV Au+Au collisions (10-15% central).	
112		Parameters extracted from the chi-square goodness-of-fit test, as well as other	
113		statistics, are shown in the box on the top right. . . . .	32
114	6.1	$(dE_T/d\eta)/0.5N_{part}$ at midrapidity as a function of $N_{part}$ for different collision	
115		energies. . . . .	36



116	6.2	$(dE_T/dy)/0.5N_{part}$ at midrapidity as a function of $N_{part}$ for different collision	
117		energies. . . . .	37
118	6.3	$(dE_T/d\eta)/(dN_{ch}/d\eta)$ at midrapidity as a function of $N_{part}$ for different collision	
119		energies. . . . .	38
120	6.4	$(dE_T/dy)/(dN_{ch}/dy)$ at midrapidity as a function of $N_{part}$ for different collision	
121		energies. . . . .	39
122	6.5	$(dE_T/d\eta)/0.5N_{part}$ at midrapidity as a function of $\sqrt{s_{NN}}$ in logarithmic scale	
123		for different centralities. . . . .	40
124	6.6	$(dE_T/dy)/0.5N_{part}$ at midrapidity as a function of $\sqrt{s_{NN}}$ for different centralities.	41
125	6.7	$(dE_T/d\eta)/(dN_{ch}/d\eta)$ at midrapidity as a function of $\sqrt{s_{NN}}$ for different	
126		centralities. . . . .	42
127	6.8	$(dE_T/dy)/(dN_{ch}/dy)$ at midrapidity as a function of $\sqrt{s_{NN}}$ for different	
128		centralities. . . . .	43
129	6.9	$\frac{dE_T}{d\eta}/0.5N_{part}$ for 0-5% central collisions at midrapidity as a function of $\sqrt{s_{NN}}$ .	
130		The PHENIX data are from [19]. The error bars represent the total statistical	
131		and systematic uncertainties. . . . .	44

# Chapter 1

## Introduction

The Big Bang model is based on observational evidence, such as the cosmic microwave background radiation and the cosmological expansion [20, 21], and suggests that at the beginning the universe must have been at a state of extremely high density and temperature. As the universe expanded, it went through several stages of cooling characterized by the formation of matter with different compositions.

The Large Hadron Collider (LHC) at CERN and the Relativistic Heavy Ion Collider (RHIC) at the Brookhaven National Laboratory have the ability to collide heavy nuclei, such as those of gold and uranium, at nearly the speed of light, reaching temperatures of trillions of degrees Celcius. These laboratories have provided evidence of the formation of an exotic state of matter, called the quark-gluon plasma (QGP) [22, 23]. It only exists for a brief amount of time after such collisions and instantly freezes out into a plethora of new particles, which carry the signatures we can use to deduct QGP properties. Its properties suggest that it should be similar to the matter that existed within microseconds of the genesis of the universe, about 13.8 billion years ago [24, 25, 26].

One of the methods to probe the properties of this matter is by analyzing the conversion of the beam-direction energy at the time of collision into transverse energy after the collision. These measurements can be used to estimate the energy density of the QGP. This analysis is generally done by using data from the calorimeters (section 4.2.1) placed around the collision site. In this thesis, I use the data collected by tracking detectors (section 4.3.1), instead of the conventional calorimeters, to calculate the transverse energy.

154 This thesis is structured as follows. Chapter 2 touches on the theoretial background  
155 associated with the concept of the quark-gluon plasma. In chapter 3, I summarize the  
156 experimental concepts pertaining to relativistic heavy-ion collisions and the production and  
157 detection of QGP. Chapter 4 consists of the formalism of the measurement of transverse  
158 energy using calorimeters as well as tracking detectors. It also describes what has been done  
159 using calorimeters. Chapter 5 describes the data used to perform the analysis in this thesis  
160 and notes the relevant details of the analysis. In chapter 6, I present the results and compare  
161 them to the ones in literature obtained using a different method. Chapter 7 concludes the  
162 thesis and discusses its implications. Finally, in chapter ??, I present arguments on what  
163 can be done in the future using the results of and the software developed for this analysis.

# Chapter 2

## Theoretical Background

### 2.1 Quantum Chromodynamics

The strong force is one of the four fundamental interactions in physics. At large scales, it is also known as the residual strong force, and it is responsible for binding the nucleons together to give the nucleus its structure. At smaller scales, it is called the fundamental nuclear force, and it binds the fundamental units of subnuclear matter, the quarks, together to form the nucleons. The force carriers of the interaction are the mesons at the former scale and the gluons at the latter. The electrodynamic interaction between charged particles such as protons and electrons is described by quantum electrodynamics (QED) as mediated by photons; the strong interaction, albeit more complicated, is explained under the framework of quantum chromodynamics (QCD) [27, 28]. The quarks and gluons of QCD are collectively known as partons. Gluons are the gauge bosons of the Yang-Mills theory.

The Yang-Mills theory is a non-Abelian gauge theory. It has a Lagrangian with several degrees of freedom, some of which are redundant and need to be gauged. This is done by a mathematical treatment as prescribed under a gauge theory [29]. The gauge theory associated with the Yang-Mills theory is based on the  $SU(N)$  group. It is non-Abelian as represented by the non-commutative transformations. QCD is a gauge theory that describes the application of the  $SU(3)$  symmetry transformations on color charges, namely red, blue, and green. The electroweak theory, which describes the electromagnetic as well as nuclear

184 weak interactions, can be formalized under the gauge group  $SU(2) \times U(1)$ . Together, they  
185 form the  $SU(3) \times SU(2) \times (U(1))$  gauge theory called the standard model.

186 One of the ways QCD is different from QED is the confinement of partons. In QED, the  
187 fundamental particles are bound together by the Coulomb potential, which diminishes with  
188 distance between the charge-carrying particles, as demonstrated by the relation 2.1:

$$V_C \propto \frac{1}{r} \tag{2.1}$$

189 where  $V_C$  is the Coulomb potential, and  $r$  is the spatial separation between the particles.  
190 This means that bound QED particles can be isolated by increasing their spatial separation.  
191 The QCD potential, on the other hand, has an extra linear term in it, which means that  
192 the potential increases linearly with distance at large distances, and so an infinite amount of  
193 energy is required to separate quarks [30]. Hence, we never observe isolated quarks and they  
194 are said to be confined, not just bound, to form composite structures called hadrons [31].  
195 A quark and an anti-quark forms a meson and three quarks forms a baryon. In addition to  
196 having a color charge, a quark also carries a flavor. There are six different quarks based on  
197 the flavors they carry: up, down, top, bottom, beauty, and strange.

## 198 2.2 Phase Transitions

199 In everyday life, we observe matter existing in four distinct phases: solid, liquid, gas, and  
200 plasma. Changes in physical conditions can lead to a transition from one of these phases  
201 to another, exemplified by the commonly observed conversion of ice to water. Distinctions  
202 among the various phases can be represented in a chart called the phase diagram.

203 The phase diagram consists of thermodynamic observables such as temperature and  
204 density on its axes. Curves in the phase diagram represent boundaries of physical conditions  
205 separating one phase from another: crossing a boundary represents an abrupt transition from  
206 one phase to another. This abruptness is mathematically characterized by the discontinuity  
207 in the change of the derivative of the free energy – a thermodynamic variable – with respect  
208 to the physical quantities in the axes. Such an abrupt transition is called a first-order phase

transition. Along the boundary represented by the curve, there can be a point beyond which the phase transition is continuous instead of being abrupt, and the distinction between two phases is not clear. This point is called a critical point, and the phase transition that takes place beyond this point is called a crossover.

One of the main focuses of current experimental and theoretical nuclear physics research is the study of the phase diagram of strongly interacting matter at a range of temperatures and baryon chemical potentials. In experiments involving the collisions of heavy ions at high and low energies, different regions of the phase diagram can be probed by varying the collision energy [19]. For instance, the high-baryon chemical potential regime corresponds to lower beam energies and higher temperatures correspond to higher beam energies. The results of these experiments and model calculations can be used to study the possibilities and signatures of transitions in the QCD phase diagram.

A schematic representing the QCD phase diagram as a function of the temperature ( $T$ ) and quark chemical potential ( $\mu$ ) is shown in Figure 2.1 [2]. A crossover is predicted at low baryon chemical potentials (close to baryon-antibaryon symmetry) and high temperatures reminiscent of the early universe. Methods to study this region of the phase space will be explored in this thesis. At low temperatures and high net baryon densities, loose predictions have been made regarding the existence of exotic phases of high density matter, and programs, such as the Compressed Baryonic Matter experiment at the Facility for Antiproton and Ion Research in Germany, are being designed to study this region of the phase diagram [32].

## 2.3 Quark-Gluon Plasma

The confinement of quarks into the hadronic phase of QCD matter, as described in section 2.1, has its limitations. At very high densities, when the wave function of a single hadron overlaps with the spatial regions covered by multiple such hadrons, it is impossible to classify which pair or triplet of quarks belongs to which meson or baryon. As long as a particular quark is close enough to the other quarks in the volume, it is deconfined in such a way that it can freely move anywhere in the volume [31]. QCD predicts such phase transition, at

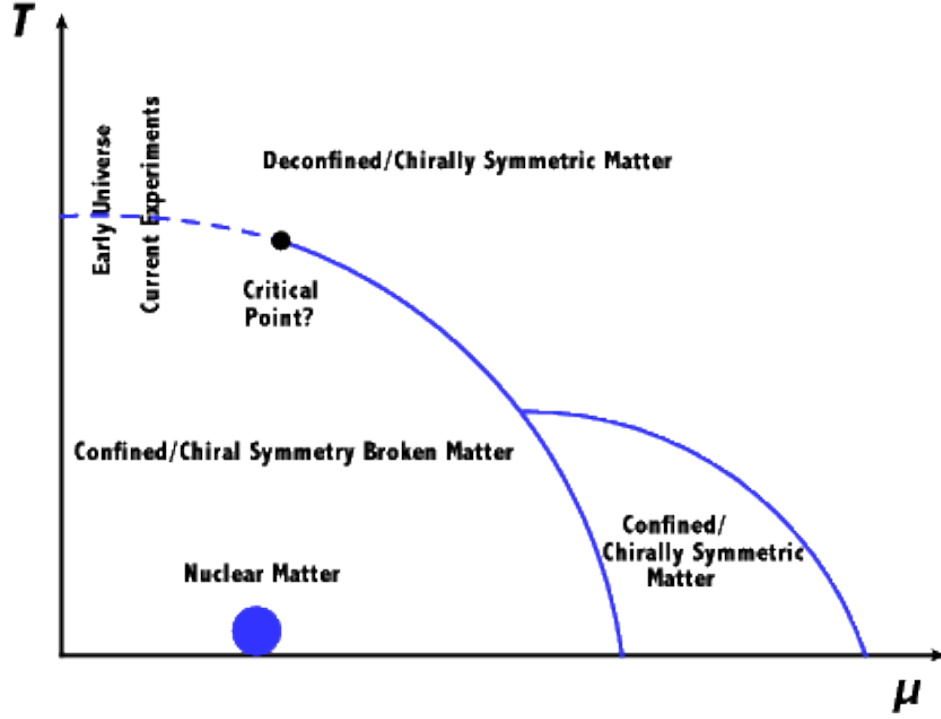


**Figure 2.1:** Schematic of the QCD phase diagram [2].

237 energy densities above  $0.2\text{-}1 \text{ GeV}/\text{fm}^3$  [33] and around a critical temperature of about 160  
 238 MeV [34], of strongly interacting matter to a phase with quarks and gluons in thermal and  
 239 chemical equilibrium representing the relevant degrees of freedom. This deconfined state  
 240 of quarks and gluons is termed the quark-gluon plasma (QGP) in analogy to the quantum  
 241 electrodynamical plasma phase of matter. The QGP has been found to behave like an almost  
 242 perfect fluid [35]

## Chapter 3

# Relativistic Heavy Ion Collisions

The experimental evidence for the QGP comes from the collisions of heavy nuclei. Some of its signatures are described in section 3.5. Physicists proposed the existence of such matter since as far back as 1984, when nuclei were accelerated and collided with stationary targets [23]. They were able to agree on a conclusive discovery of this matter during the 2000s, after colliding accelerated nuclei with other such nuclei or smaller species (protons, deuterons) at unprecedented energies and with improved detection schemes [36]. With further increases in collision energies and enhancements in detector technology, modern accelerator facilities provided additional evidence and estimates of some of the properties as well as the dynamics of the evolution of the QGP. The following sections describe two such facilities, the physics of the collisions, and what happens after the collisions.

### 3.1 RHIC and LHC

The Relativistic Heavy Ion Collider (RHIC) is located in Upton, New York in the premises of the Brookhaven National Laboratory (BNL). Its construction started in 1991 and was completed in 1999. Figure 3.1 shows the layout, at the time of construction, of the collider along with the Alternating Gradient Synchrotron (AGS) complex and the locations of the original four detectors: Solenoidal Tracker At RHIC (STAR), Pioneering High Energy Nuclear Interaction eXperiment (PHENIX), Phobos, and BRAHMS (Broad Range Hadron Magnetic Spectrometers). Phobos, BRAHMS, and PHENIX were decommissioned after the



completion of their science objectives, but STAR is still operational. The AGS was part of BNL before the construction of the RHIC, and its capabilities were augmented with the construction of the AGS Booster in 1991.

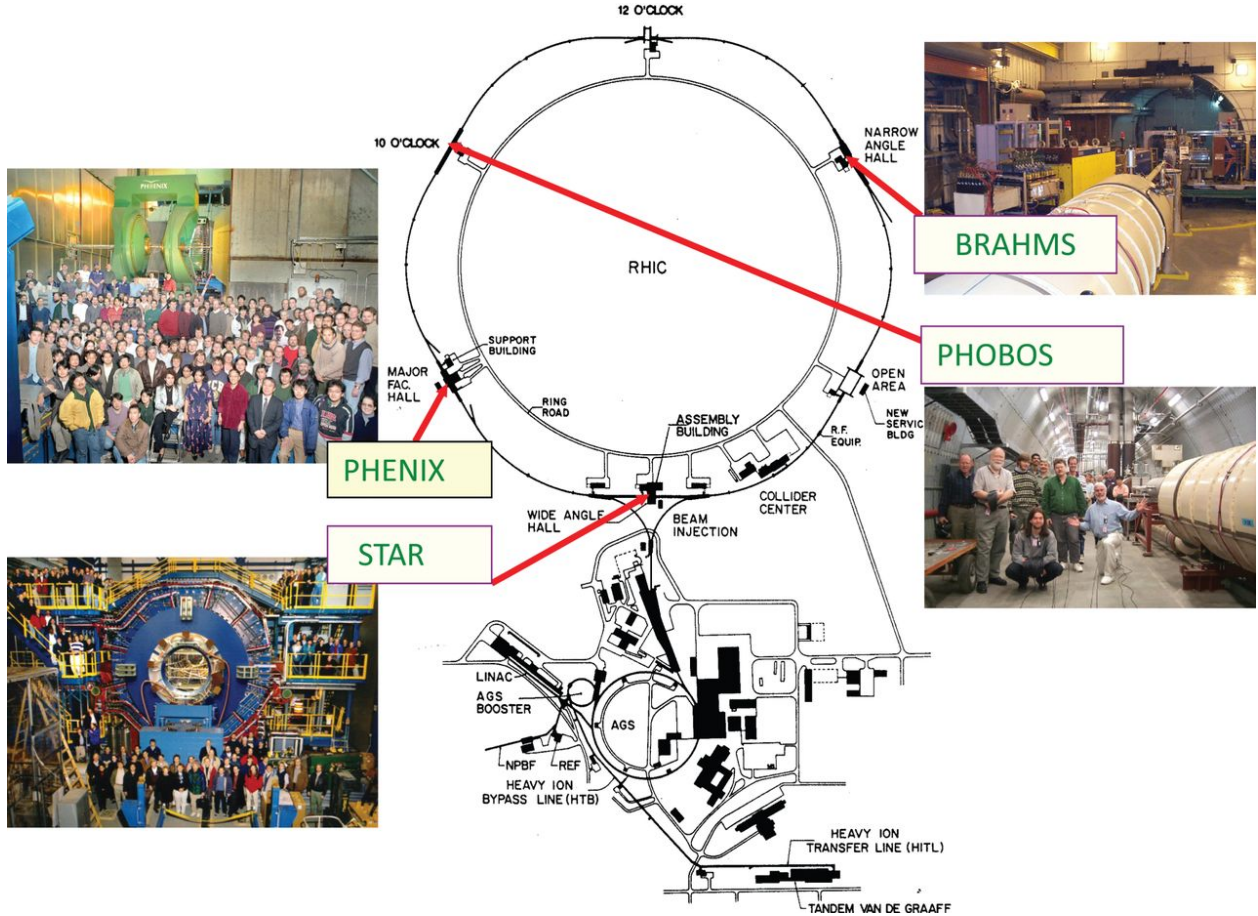


**Figure 3.1:** Initial layout of the RHIC [3].

Heavy ion beams in RHIC are created in a series of steps before collision. In case of gold ions, a pulsed sputter source produces negatively charged ions, which are stripped of some of their electrons with a foil on the positive end of the high-voltage Tandem Van de Graaff. The ions are now positively charged and are accelerated to 1MeV/u toward the negative terminal of the Tandem. Upon exiting it, some more stripping takes place. The bending magnets then selectively deliver +32 charge states of the ions to the Booster Synchrotron, which accelerates them to 95MeV/u and strips them to a +77 charge state before injecting them to the AGS. The AGS accelerates them to 10.8 GeV/u and strips them of the remaining two electrons at the exit. The gold ions are then injected through the AGS-to-RHIC Beam Transfer Line to

the two RHIC rings. These rings carry beams moving in opposite directions and intersect at six symmetric locations in the 3.8 km circumference. The original four detectors are located in four of these six locations where the beams undergo head-on collisions.

The Large Hadron Collider (LHC) is located underground (between 45m and 170m) beneath the France-Switzerland border near the city of Geneva. The two rings of the collider were constructed between 1998 and 2008 by the European Organization for Nuclear Research (CERN) in the 26.7 km circular tunnel originally housing CERN's Large Electron-Positron collider. Analogous to the RHIC, the LHC gets its beams prepared by a series of machines in the CERN accelerator complex. The collisions occur at the locations of the four big LHC experiments: Compact Muon Solenoid (CMS), A Toroidal LHC ApparatuS (ATLAS), Large Hadron Collider beauty (LHCb) experiment, and A Large Ion Collider Experiment (ALICE). ALICE is dedicated to the study of heavy-ion collisions [37].

## 3.2 Collision Energy and Geometry

What happens in the aftermath of a collision depends on how much energy is available at the time of the collision as well as the geometry of the collision. The collision energy is determined by the collider configuration. The geometry of the collision is deduced as the collision *centrality*, as described later in this section, through the estimation of the charged particle multiplicities ( $N_{ch}$ ) resulting from the collisions.

In collision experiments, it is convenient to use a reference frame in which the net momentum of the pair of colliding species is zero. This frame is called the center-of-mass frame. In this frame, the total energy of the species in the two beams is a function of the number of nucleons and the center-of-mass energy per nucleon. The collision energy is reported as the center-of-mass energy per nucleon pair,  $\sqrt{s_{NN}}$ .

RHIC has the unique capability of colliding species at a range of energies spanning almost two orders of magnitude. Table 3.1 lists the collision energies produced so far at RHIC for various collision systems. The LHC boasts the highest amount of collision energy for any collider on earth. It collided species (p+p, p+A, Pb+Pb) at a center of mass energy up to

302 2.76 TeV per nucleon pair at the end of 2010. At the end of 2015, 5.02 TeV Pb+Pb and 13  
303 TeV p+p collisions were successfully completed [22].

Collision system	$\sqrt{s_{NN}}(GeV)$
p+p	200, 510
d+Au	19.6, 39, 62.4, 200
Cu+Cu	62.4
Cu+Au	200
p+Au	200
$^3\text{He}+\text{Au}$	200
Au+Au	7, 7.7, 9, 20, 62, 130, 200

**Table 3.1:** Colliding species and associated collision energies at RHIC [1].

304 In general, any collision between two nuclei is not perfectly head-on. Some collisions are  
305 close to being head-on and are called central collisions. Some are glancing and are called  
306 peripheral collisions. By convention, 0% is the centrality of a perfectly head-on collision and  
307 100% is that of the least head-on, i.e., the most peripheral collision. More central collisions  
308 generally produce more particles [4].

309 The centrality is estimated through a model-based correlation between  $N_{ch}$  and the  
310 impact parameter, defined as the distance between the centers of the two nuclei at the  
311 time of their maximum overlap. The Monte Carlo based model, for instance, assumes that  
312 all nucleons travel in straight lines along the beam direction [38] and that they collide if they  
313 overlap [39].  $N_{ch}$  is assumed to scale with the number of participants and the number of  
314 binary collisions. The distribution of this quantity is then fit to the data and the fraction of  
315 the overlap is estimated from the observed  $N_{ch}$  value. 5% of all collisions with the highest  
316  $N_{ch}$  values, for example, are then referred to as being 0-5% central [4].

317 Figure 3.2 illustrates the aftermath of a mid-central collision, i.e, a collision in which  
318 about half of the volume of each of the nuclei intersects the other.

319 The collision of two nuclei can be modeled as collisions of the constituents that make  
320 up the nuclei. The nucleons that take part in the collisions and are called participants.  
321 The rest of the nucleons are known as spectators. Figure 3.3 illustrates the distribution of  
322 participants and spectators in two colliding nuclei.

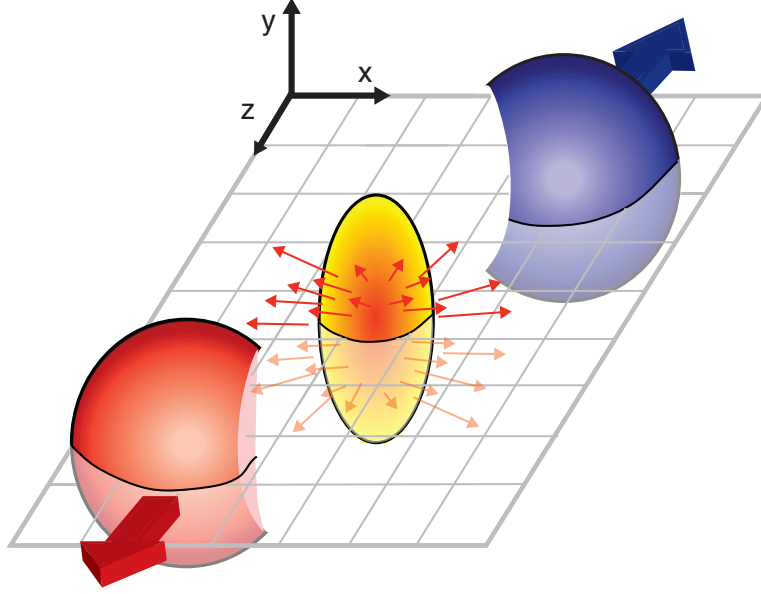


**Figure 3.2:** An illustration of a mid-central collision of two nuclei traveling in the  $z$  direction. The  $X$ -axis is parallel to the line joining the centers of the two nuclei at the time of collision [4].

### 3.3 QGP Evolution

The evolution of the QGP is shown in a lightcone diagram in figure 3.4 [4]. The initial state of the colliding nuclei is not precisely known and is the topic of research for upcoming experiments. During the collision, the participants scatter off of each other while the spectators keep traveling almost unperturbed in their original direction. The immediate aftermath of a central collision of heavy ions at RHIC and LHC energies is the formation of a hot fireball. This fireball evolves in time to form a liquid-like medium of quarks and gluons. This medium attains a local equilibrium and remains in such a state, depending on the collision energy, for about 1-10 fm/c. This equilibrium is broken as the liquid QGP evolves by expanding and cooling to attain a density and temperature at which the medium undergoes hadronization followed by a chemical freeze-out to form a hadron gas. The particle ratios are fixed after the chemical freeze-out. Collisions between the constituents of this gas become scant as it evolves with further expansion and cooling, and the hadrons undergo a thermal freeze-out to attain their final energies and momenta [4].

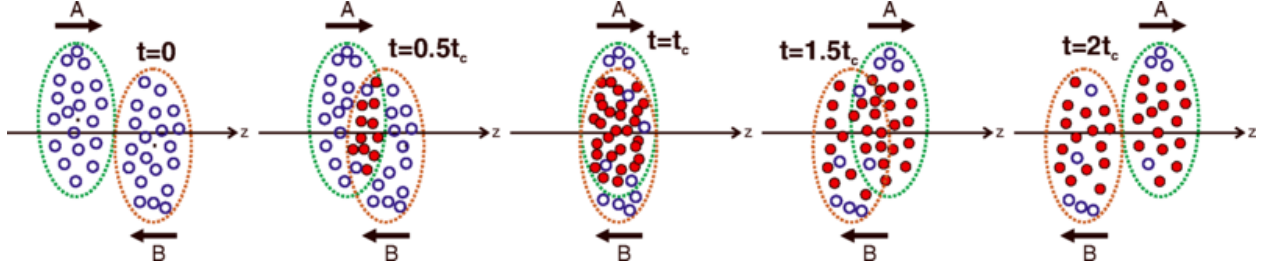


**Figure 3.3:** An illustration of a collision consisting of participants (solid red) and spectators (open blue) within the colliding nuclei labeled A and B.  $t_c$  denotes the time of maximum overlap of the two nuclei. The apparent narrowing of the volumes of the nuclei in the  $z$ -direction is due to Lorentz contraction [5].

### 3.4 Detection of Collision Products

Detectors are placed around the collision site to perform measurements on the final state particles emitting from the thermal freeze-out of the medium. These measurements typically include the reconstruction of the particle tracks, estimation of the types of particles, and the momenta and energies they carry.

Generally, a tracking detector surrounds the collision site, and there are particle identifiers followed by calorimeters around it. A magnetic field is applied parallel to the beam direction around the collision site. Due to this orientation of the magnetic field, the spectators traveling parallel to it move roughly undeflected and the final state charged particles with components of velocity transverse to the beam axis get deflected around the beam axis with radius given by

$$r = \frac{p_T}{qB}, \quad (3.1)$$

where  $p_T$  is the transverse momentum of the particle,  $q$  is its electric charge, and  $B$  is the applied magnetic field. Two kinds of detectors most relevant to this thesis, tracking detectors and calorimeters, are described in chapter 4.

### 3.5 Detection of QGP Signatures

The existence and properties of the QGP in the aftermath of high-energy heavy-ion collisions can be probed using different techniques relevant to several theoretical characteristics of the

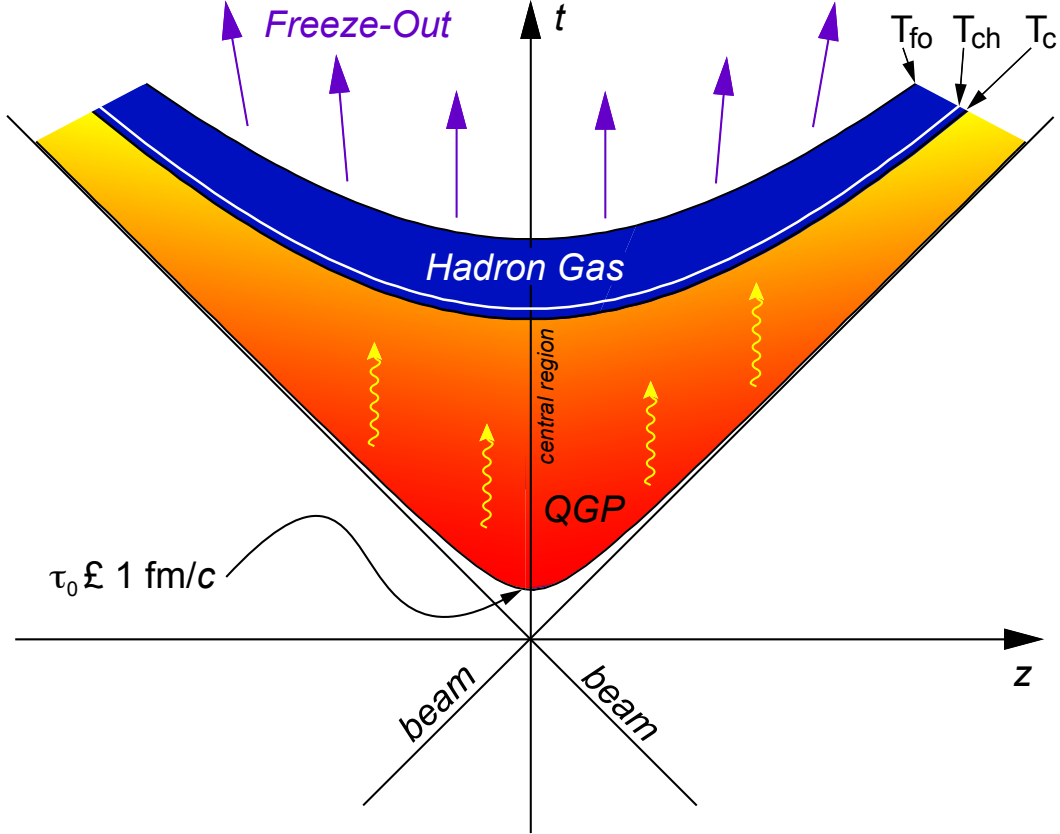


**Figure 3.4:** Evolution of the QGP represented in a lightcone diagram.  $\tau_0$  denotes the formation time of the QGP.  $T_c$  is the critical temperature of the transition from the QGP to the hadron gas phase.  $T_{ch}$  and  $T_{fo}$  stand for the temperatures at, respectively, chemical freeze-out and thermal freeze-out [4].

medium. No signature can alone be used to claim the production of the QGP, and some of the probes, which should be interpreted together, are described below.

### 3.5.1 Bjorken Energy Density

In 1983, J.D. Bjorken[40] prescribed a formula to use the final state particles to estimate the initial energy density,  $\epsilon_0$ , in a nucleus-nucleus collision. With slight changes in the original formula, the energy density is estimated by:

$$\epsilon_0 = \frac{1}{\tau_0 A_T} \left\langle \frac{dE_T}{dy} \right\rangle, \quad (3.2)$$

360 where  $\tau_0$  is the formation time of the QGP,  $A_T$  is the transverse area of the intersection  
 361 of the two nuclei, and  $\langle \frac{dE_T}{dy} \rangle$  is the mean transverse energy per unit rapidity.  $\tau_0$  is model-  
 362 dependent and is normally estimated to be  $1fm/c$ .  $A_T$  depends on the centrality of the  
 363 collision and can be estimated using the Glauber model discussed earlier.  $\langle \frac{dE_T}{dy} \rangle$  is found  
 364 from the measurement of the transverse energy carried by the final state particles from the  
 365 collision and is the central theme of this thesis. Details about it are in the following chapters.  
 366 The estimate of the initial energy density from the Bjorken formula is an underestimate of  
 367 the maximum energy density because the measured  $dE_T/dy$  is an average over the system  
 368 as it undergoes expansion and cooling. It can be compared with the QCD prediction of the  
 369 critical energy density [33] to check if the results from a collision imply the achievement of  
 370 the critical physical condition required for the phase transition [41]. Experiments show that  
 371 ultra-relativistic heavy ion collisions are capable of producing energy densities comfortably  
 372 higher than those predicted by QCD [33].

### 373 **3.5.2 Elliptic Flow**

374 The evolution of the medium produced in relativistic heavy ion collisions can be well  
 375 described under the framework of relativistic hydrodynamics [42, 43]. This description  
 376 indicates the presence of a collective flow of a locally thermalized liquid. The angular  
 377 distribution of the momenta of the final state particles emitted out of the collectively flowing  
 378 system can be decomposed into a Fourier expansion in its azimuthal components. The  
 379 second harmonic coefficient,  $\nu_2(y, p_T)$ , of this decomposition characterizes what is known as  
 380 the elliptic flow [44]. The magnitude of the elliptic flow from a non-central collision represents  
 381 the anisotropy in azimuthal momentum space of the thermalized post-collision system [45].  
 382 The elliptic flow of the medium, as a function of the momentum or the kinetic energy in the  
 383 transverse direction, points towards quarks, rather than hadrons, being the relevant degrees  
 384 of freedom in the QGP. Figure 3.5 shows  $v_2$  as a function of the transverse momentum  
 385 and the transverse kinetic energy for identified particles. The spectra scale consistently at  
 386 lower values of both  $p_T$  and  $KE_T$ . However, they branch out as mesons and baryons at  
 387 higher values:  $p_T \gtrsim 2GeV/c$  and  $KE_T \gtrsim 1GeV$ . Figure 3.6, on the other hand, is similar to  
 388 figure 3.5, with the exception that both the axes have quantities that are normalized by the

number of quarks,  $n_q$ . In this case, the  $KE_T$  spectra strongly exhibits a scaling which is more comprehensively consistent with the number of quarks than in case of figure 3.5. This universal quark-number scaling can be interpreted as the degrees of freedom of the system being quark-like [6].

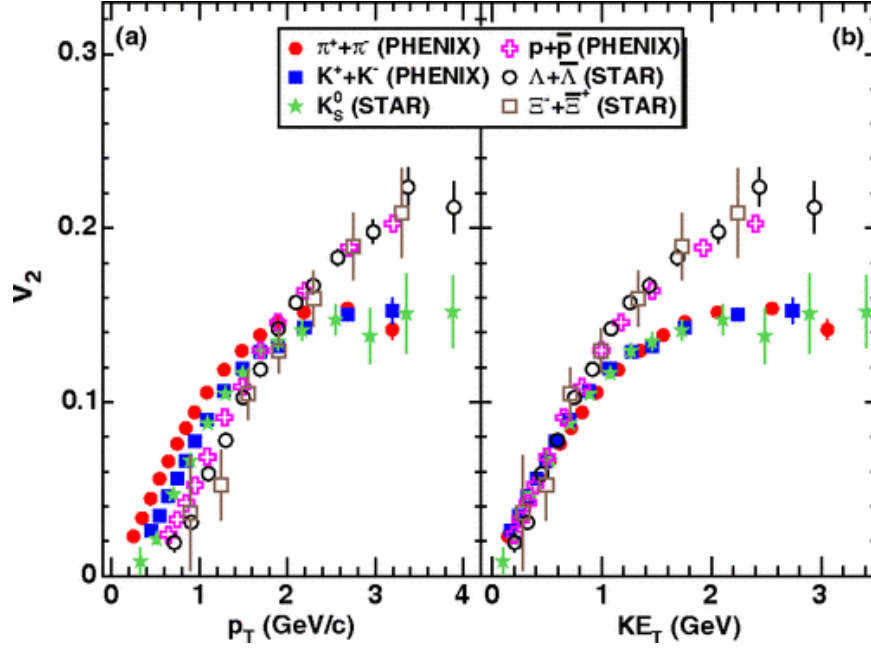


**Figure 3.5:** Minimum-bias Au+Au ( $\sqrt{s_{NN}} = 200\text{GeV}$ ) elliptic flow spectra for identified particles: (a)  $v_2$  vs  $p_T$  and (b)  $v_2$  vs  $KE_T$  [6].

### 3.5.3 Prompt and Thermal Photons

Most of the photons observed after relativistic heavy ion collisions are the results of the decay of the neutral pion into two gammas. When these photons are subtracted from the observations, the remaining photons are called direct photons [46]. These direct photons are produced within the fireball via different mechanisms as discussed below.

In the QGP, a quark and an antiquark can annihilate to produce a photon and a gluon. It is also possible for the pair to annihilate and produce two photons, but the probability of this process is smaller than the former by about two orders of magnitude. Furthermore, a quark (or an antiquark) can interact with a gluon to produce an antiquark (or a quark) and a photon, a process analogous to Compton scattering in QED. The photons produced from the hard scattering processes between the partons are called prompt photons, and



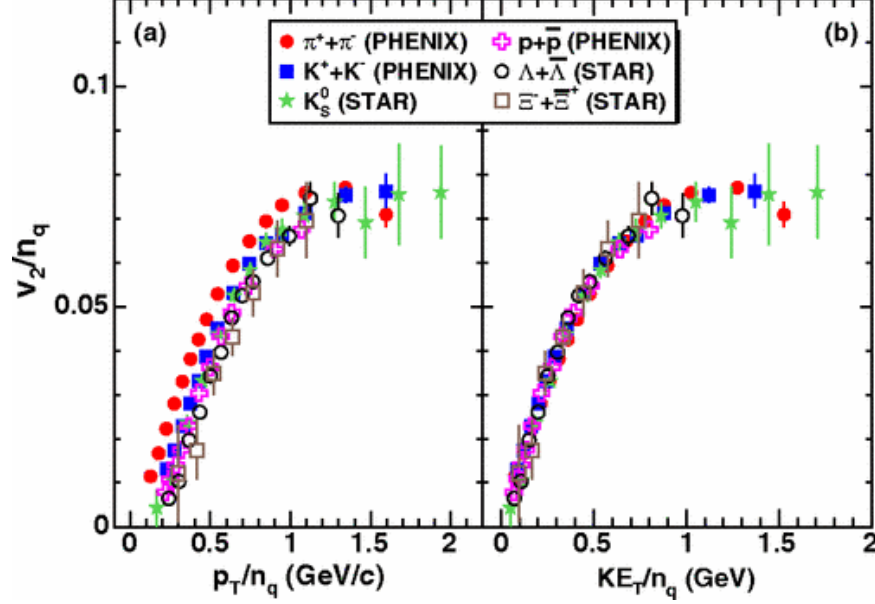


**Figure 3.6:** Minimum-bias Au+Au ( $\sqrt{s_{NN}} = 200\text{GeV}$ ) elliptic flow spectra for identified particles: (a)  $\frac{v_2}{n_q}$  vs  $\frac{p_T}{n_q}$  and (b)  $\frac{v_2}{n_q}$  vs  $\frac{KE_T}{n_q}$  [6].

404 their multiplicity scales with the number of binary collisions. Photons can also be produced  
 405 due to scatterings of partons within the thermalized medium, and these photons are called  
 406 thermal photons. The nature of the  $p_T$  distribution is different in this case as the emission  
 407 process mimics blackbody radiation. This difference helps distinguish these photons from  
 408 the direct photons produced by partonic interactions. Just like the leptons described in  
 409 the previous section, the photons produced in the QGP can only interact with the medium  
 410 electromagnetically. Therefore, they undergo minimal scattering before being detected, and  
 411 hence can be used to probe the thermodynamical state of the medium at the time of their  
 412 creation [7, 46, 47].

### 413 3.5.4 Strangeness Enhancement

414 The interacting nuclei carry no net strangeness before colliding, and so an observation of  
 415 strange and multi-strange particles after the collision can be used to probe the properties of  
 416 the post-collision medium [48]. Strangeness can also be produced in hadron-hadron collisions.  
 417 However, it is enhanced in nucleus-nucleus collisions [49]. This is interesting because it  
 418 possibly indicates a restoration of chiral symmetry, which is a topic of ongoing research:

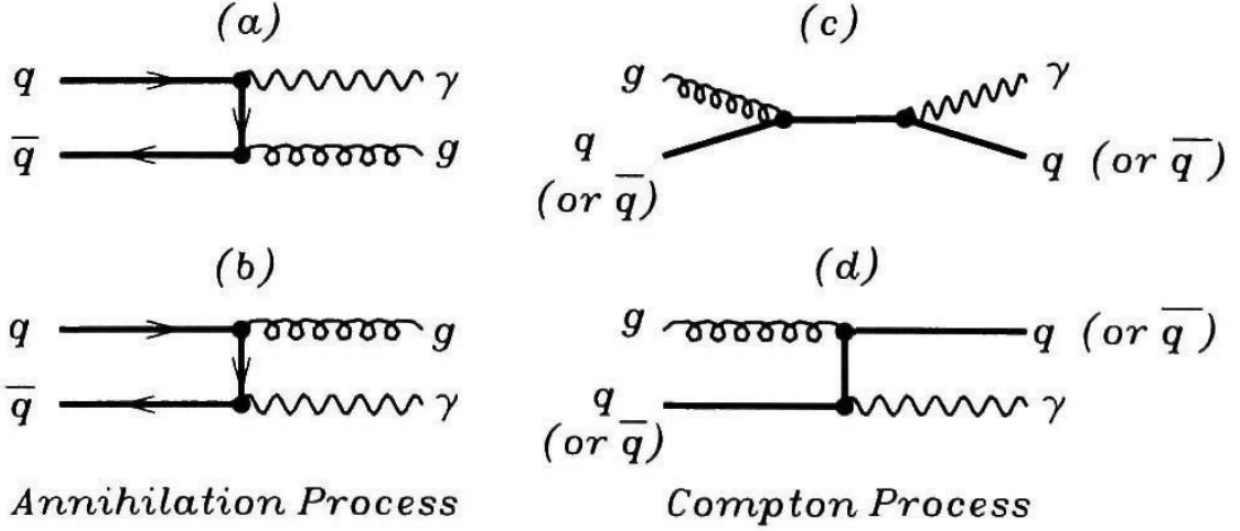


**Figure 3.7:** Feynman diagram representing the production of photons from quarks and gluons. (a) and (b) represent annihilation processes, whereas (c) and (d) represent Compton processes [7].

in the zero baryon chemical potential limit, lattice QCD calculations reveal a transition of QCD matter between a phase with broken and one with restored chiral symmetry [50]. Chiral symmetry restoration has the implication of all the flavors of quarks losing their masses [51]. Hence, when chiral symmetry is restored, it is more feasible to produce strange quarks, for instance, which have higher masses than the light quarks, up and down, in a state of broken chiral symmetry. Chiral symmetry restoration is not the only possible reason for the production of many strange quarks. It is also feasible to produce strange quarks as long as the temperature of the system is above the strange flavor mass scale, and so it carries effects of the system temperature. This is exemplified by the ratio of the production of the strange kaons to that of the non-strange pions, which are the most abundant hadrons produced from nucleus-nucleus collisions: kaon yield increases more rapidly than pion yield does as the temperature increases [7].

### 3.5.5 Jet Quenching

A scattering event in which the participants transfer a large amount of their original momenta is called hard scattering. The products of the scatterings are called jets. In heavy-ion collisions, most hard scatterings are the results of two partons from the opposite nuclei

435 scattering off each other. These partons can lose their momenta by strongly interacting  
 436 with the enhanced gluon fields in a QGP medium. Therefore, the properties of the jets, as  
 437 carried by the final state hadrons, should be different for collisions that produce the QGP  
 438 as compared to those that do not, and hence they can be used as signatures and probes of  
 439 QGP. Figure 3.8 illustrates the quenching of jets that have to travel long distances in the  
 medium.

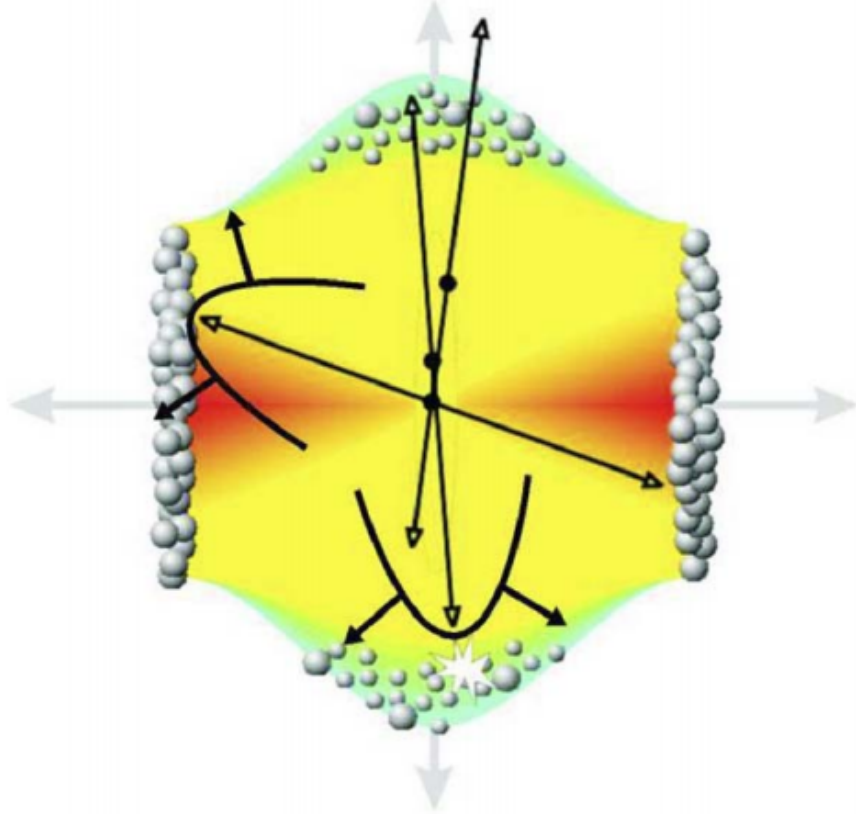


**Figure 3.8:** Illustration of jet quenching. Two jets are produced from each of the hard scatterings occurring at the locations of the solid dots. Jets originating closer to the initial surface are more probable to propagate outside the medium, as shown. Jets opposite to them interact with the medium, losing their energy and resulting in bow front shock waves [8].

440

441 The nuclear modification factor,  $R_{AA}$ , is the ratio of the cross section for particle  
 442 production in nucleus-nucleus collisions scaled by the number of binary nucleon-nucleon  
 443 collisions divided by the cross section in proton-proton collisions. It is shown in Fig. 3.9 for  
 444 several different particle species, demonstrating substantial suppression of high momentum  
 445 particles. This shows that the medium is nearly opaque to colored probes.

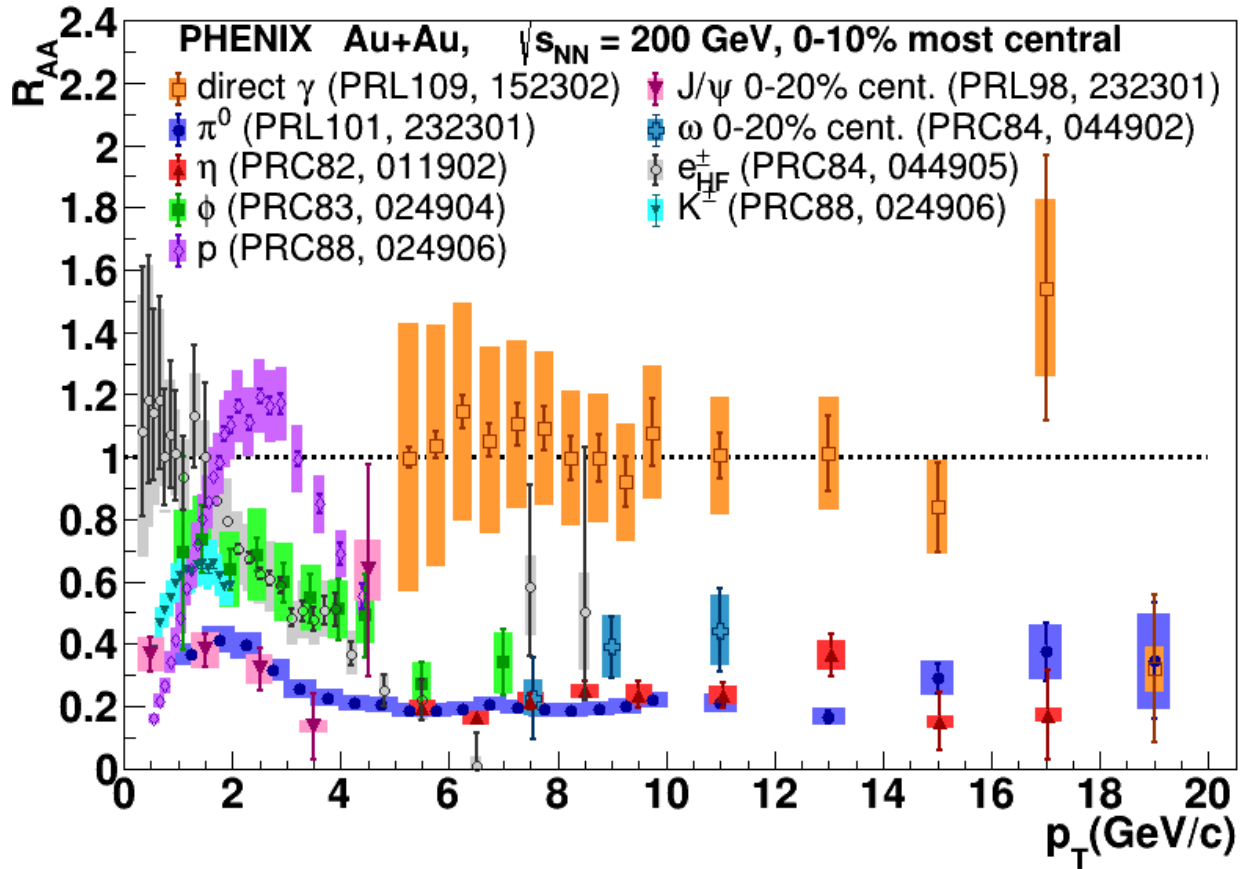


**Figure 3.9:**  $R_{AA}$  from PHENIX for direct photons [9],  $\pi^0$  [10],  $\eta$  [11],  $\phi$  [12],  $p$  [13],  $J/\psi$  [14],  $\omega$  [15],  $e^\pm$  from heavy flavor decays [16], and  $K^\pm$  [13]. This demonstrates that colored probes (high- $p_T$  final state hadrons) are suppressed while electroweak probes (direct photons) are not at RHIC.

### 3.6 The Beam Energy Scan Program

The RHIC, in 2010, started a multi-phase Beam Energy Scan (BES) program to study the QCD phase diagram. Between 2010 and 2011, during the exploratory phase I of the BES program, the collider provided Au+Au collisions at 7.7, 11.5 (not completed in PHENIX), 19.6, 27, and 39 GeV. Together with the data formerly collected by the RHIC at higher collision energies, BES phase I data can scan the interval from 450 MeV to 20 MeV in  $\mu_B$  space [52, 53]. One of the things that can be studied with the data associated with this region of the phase space is the possibility of a “turn-off of new phenomena already established at higher RHIC energies” [52]. Results corresponding to the high- $\mu_B$  region might provide evidence of a first order phase transition, and possibly the critical point [53].

456 The manifestation of such phenomena might be in terms of the fluctuations or other  
457 properties of the post-collision system. One can, for instance, study the scaling of the energy  
458 density after the collision with the longitudinal energy at the time of the collision,  $\sqrt{s_{NN}}$ ,  
459 for which one needs to measure the transverse energy. This can be done in multiple ways  
460 using a detector like STAR or PHENIX that is made up of sub-systems such as the Time  
461 Of Flight (TOF) detectors, Time Projection Chambers (TPCs)/Time Expansion Chambers,  
462 and calorimeters. The next chapter describes the measurement of transverse energy using  
463 BES data from PHENIX calorimeters. Also, the next chapter and the ones after it contain  
464 the procedures and the results of the analysis of the BES data from STAR using the identified  
465 particle spectra.

## Chapter 4

# Measurement of Transverse Energy

This chapter introduces the definitions of transverse energy, ways to measure it using different detectors, and particular examples for the detectors at the RHIC.

### 4.1 Definition of Transverse Energy

The transverse energy,  $E_T$ , from a collision can be defined as the sum of the transverse masses,  $m_T$ , of all the particles produced in the collision, i.e.,

$$E_T \equiv \sum_i m_{T,i} \quad (4.1)$$

with

$$m_T \equiv \sqrt{p_T^2 + m^2} \quad (4.2)$$

where  $m$  is the rest mass of the particle and  $p_T$  is its transverse momentum. Using this definition to calculate the  $E_T$  requires perfect identification of all the particles. It has not been possible to do so in experiments, and so a more feasible, operational definition of  $E_T$  is used. A commonly accepted definition in the case of calorimetric measurements is [54, 35]:

$$E_T = \sum_i E_i \sin \theta_i, \quad (4.3)$$

478

$$\frac{dE_T}{d\eta} = \sin\theta \frac{dE}{d\eta}, \quad (4.4)$$

479 where the index  $i$  runs over all the particles going into a fixed solid angle for each event,  
 480  $\theta$  is the polar angle, i.e, the angle with respect to the beam axis,  $\eta$  is the pseudorapidity  
 481 defined as

$$\eta \equiv -\ln \tan \frac{\theta}{2}, \quad (4.5)$$

482 and  $E_i$  is the energy deposited in the calorimeter by the  $i^{th}$  particle.  $E_i$  is considered to be,  
 483 by convention [55], the following

$$E_i = \begin{cases} E_i^{tot} - m_0 & \text{for baryons} \\ E_i^{tot} + m_0 & \text{for anti-baryons} \\ E_i^{tot} & \text{otherwise} \end{cases} \quad (4.6)$$

484 where  $E_i^{tot}$  is the total energy of the  $i^{th}$  particle defined canonically as

$$E^{tot} \equiv \sqrt{p^2 + m_0^2} \quad (4.7)$$

485 and  $m_0$  is the particle's rest mass.

486  $E_i$  given by equation 4.6 is what would be observed by a calorimeter. In order to  
 487 account for the portion of the emitted transverse energy not detected or overestimated by  
 488 the calorimeters, corrections are made based on simulations.

## 489 **4.2 $E_T$ Measurement with Calorimeters**

### 490 **4.2.1 Calorimeter**

491 A calorimeter in a particle or nuclear physics experiment is a device used to measure the  
 492 energy carried by a particle by analyzing the signal generated by the shower of particles  
 493 produced by the interaction of the incoming particle with the material of the device [56].  
 494 In theory, a single calorimeter can be made to measure the energy deposited by different

kinds of particles. However, it makes more sense to have two different kinds of calorimeters:  
 one optimized to measure the energy deposited by particles like electrons (or positrons)  
 and photons, called an electromagnetic calorimeter (EMCal), and the other optimized to  
 measure the energy deposited by hadronic particles, called a hadronic calorimeter (HCal).  
 This is because of the difference in the particle showers that these two categories of particles  
 generate. Electrons and photons mostly lose their energies in the calorimeter material via  
 bremsstrahlung, Compton scattering and pair production. They generate particle showers  
 made of electrons and photons which cannot travel much farther into the medium before  
 losing all their energies in a series of interactions producing an avalanche of sequential  
 showers. However, hadrons can interact inelastically with the nucleus generating a shower of  
 hadrons. These secondary hadrons have much larger masses than the secondary electrons in  
 the shower generated by the electrons and photons. This means they are not deflected nearly  
 as much by the electric forces in the material and travel much farther into the calorimeter.  
 For this reason, EMCals are comparably smaller in depth and are placed before the HCals  
 in a detector assembly.

## 4.2.2 $E_T$ from PHENIX Calorimetry

Adare et al. [19] uses electromagnetic calorimetry in PHENIX to analyze the transverse  
 energy corresponding to several different pairs of species colliding at a range of energies. It  
 uses the raw transverse energy measured by the EMCal,  $E_{TEMC}$ , to obtain the total  $E_T$  by  
 making corrections in three different steps.

They first scale the data by a constant factor, 4.188, calculated to account for the fiducial  
 acceptance in azimuth and pseudorapidity. The second factor is calculated to adjust for the  
 effects of the calorimeter towers that are disabled. The third factor,  $k$ , is the ratio of  $E_T$   
 and  $E_{TEMC}$  and is computed as follows:

$$k = k_{response} \times k_{inflow} \times k_{losses} \quad (4.8)$$

where  $k_{response}$  corresponds to hadronic particles only depositing a fraction of their total  
 energy while passing through the EMCal,  $k_{inflow}$  is attributable to the energy deposited



by particles coming from outside the EMCal's fiducial aperture, and  $k_{losses}$  accounts for the energy not registered in the EMCal due to energy thresholds, edge effects, and more importantly due to the particles that make it into the fiducial aperture but decay into products outside the aperture.

$k_{response}$  is estimated using simulations of event generation and particle detection. With 75% of the incident energy measured by the EMCal in the simulation,  $k_{response} = 1/(0.75) = 1.33$ . 24% of the energy measured by the EMCal is found to be associated with the 'inflow' particles, and so  $k_{inflow} = 1 - 0.24 = 0.76$ . 22% of the energy is lost due to aforementioned reasons (10% + 6% + 6%), and so  $k_{losses} = 1/(1 - 0.22) = 1.282$ . From equation 4.8, then,  $k = 1.30$ , and this factor was found to vary for all the data sets by less than 1%.

The systematic uncertainties due to several contributions (listed in Table II in [19]) are added in quadrature to obtain the total systematic uncertainties in  $dE_T/d\eta$ . The uncertainty is low for the correction related to the acceptance (2%) as compared to that for the  $k$  factor: 3% for losses and inflow and 4.5%-4.7% for the energy response.

## 4.3 $E_T$ Measurement with Tracking Detectors

Transverse energy analysis can be done using tracking detectors as well if they are able to produce measurements of other physical quantities that implicitly contain information about the transverse energy. Specifically, the charged particle multiplicity distributions with respect to the transverse momenta can be used, with assumptions involving particle ratios (section 5.3.2) and mean  $p_T$ , to calculate the particle's transverse energy. Since the corrections related to the tracking detectors are very different from those related to the calorimeters, results from the two different methods can be used to test the assumptions involved in each.

### 4.3.1 Tracking and Particle Identification

The tracking detectors in experiments such as the STAR (Solenoidal Tracker At RHIC) experiment and ALICE (A Large Ion Collider Experiment) at CERN include Time Projection Chambers (TPCs) and Time-of-Flight (TOF) detectors that can be used to measure the  $p_T$  spectra, yields, and particle ratios of the identified charged hadrons [57, 18]. The TPCs

provide measurements of particle trajectories that can be used to determine the momenta for low-momentum particles. They also provide measurements of their specific energy loss,  $\frac{dE}{dx}$ , which can be used in combination with the momenta to identify particles using the Bethe-Bloch formula [58]. The particle identification (PID) capabilities of STAR are discussed in section 4.3.3. TOF detectors cover the high-momentum part of the measurements. In ALICE, the combination of the measurements of the TPC with those of the Inner Tracking System (ITS) effectively adds the tracking length, thereby improving the resolution of the measured  $p_T$  spectrum. Details about the PID and momentum determination capabilities of the detectors in ALICE can be found in [59].

The  $p_T$  spectra, reported as  $\frac{d^2N}{dydp_T}$  as a function of  $p_T$ , can be used to calculate  $\frac{dE_T}{d\eta}$  as formulated in the following section.

### 4.3.2 Calculation of $\frac{dE_T}{d\eta}$ from $p_T$ spectra

In relativistic heavy ion collisions, rapidity ( $y$ ) is defined as follows:

$$y \equiv \frac{1}{2} \ln \frac{E + p_z}{E - p_z}, \quad (4.9)$$

where  $E$  is given by equation 4.7 and  $p_z$  is the component of the momentum parallel to the beam axis. Pseudorapidity,  $\eta$ , is just  $y$  with  $m_0 = 0$ , which leads to equation 4.5. Taking the exponential of both sides of the equation 4.5 and using Euler's formula, we get:

$$\sin \theta = \frac{1}{\cosh \eta}. \quad (4.10)$$

Hence,

$$\begin{aligned} p &= \frac{p_T}{\sin \theta} \\ &= p_T \cosh \eta, \end{aligned}$$

and so we have

$$E_T = E \sin \theta = \frac{\sqrt{p_T^2 \cosh^2 \eta + m_0^2}}{\cosh \eta} \quad (4.11)$$

The Jacobian for the transformation from  $y$ -space to  $\eta$ -space is derived to be:

$$\frac{\partial y}{\partial \eta} = \frac{p_T \cosh \eta}{\sqrt{m_0^2 + p_T^2 \cosh^2 \eta}} \quad (4.12)$$

From equations 4.11 and 4.12, we can see that the product of  $E_T$  with the Jacobian is equal to  $p_T$ . That leads to a formulation of  $\frac{dE_T}{d\eta}$  as a function of only  $\eta$  and  $p_T$ :

$$\frac{dE_T}{d\eta} = \frac{1}{2a} \int_0^{10 \text{ GeV}/c} \int_{-a}^a p_T \frac{d^2 N}{dy dp_T} d\eta dp_T \quad (4.13)$$

where  $a$  and  $-a$  are the bounds for  $\eta$ . The estimate for the upper limit of  $p_T$  makes sense in accordance with the mean  $p_T$  of the spectra being comfortably an order of magnitude less than 10 GeV/c as discussed in chapter 5. More details on the kinematic variables  $y$  and  $\eta$  are in appendix A.

### 4.3.3 Tracking Detectors in STAR

In the STAR experiment, the TPC is the primary tracking detector. It is 4.2 m long and it cylindrically encloses the accelerator beam pipe from its outside, with an inner diameter of 1 m and an outer diameter of 4 m [1]. It covers a pseudorapidity range of  $|y| < 1.8$  in all of azimuth for charged particles. It can identify particles with momenta over 100 MeV/c up to about 1 GeV/c as well as measure their momenta from 100 MeV/c to 30 GeV/c [17]. Figure 4.1 shows the PID capability of the STAR TPC for very high-multiplicity events [60]. Separation of pions from protons is demonstrated up to a little more than 1 GeV/c. At higher momenta, separating particles is more difficult because their energy loss has lower dependence on the rest mass [17]. The TOF system in STAR, with a time resolution of  $\lesssim 100$  ps, aids PID at higher momenta. However, at intermediate  $p_T$ , between  $\approx 2.0$  and 4.0 GeV/c, the TPC by itself cannot distinguish between pions and protons and the TOF by itself cannot separate pions from kaons. This problem is resolved by utilizing the fact that the dependence of the particle velocity on  $p_T$  – in case of the TPC – is different from that of the energy loss on  $p_T$  in case of the TPC; combining the results from the two, hence, makes PID feasible in this  $p_T$  range [61].

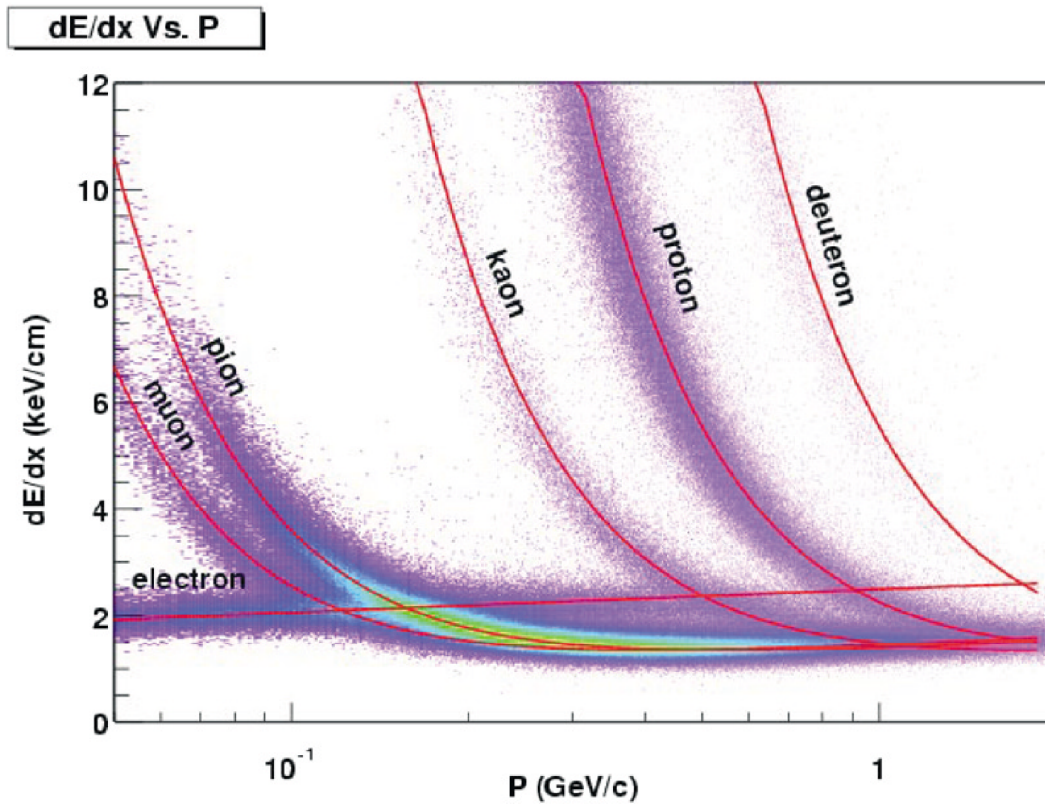


**Figure 4.1:** Energy loss distribution in the STAR TPC for primary and secondary particles [17].

# Chapter 5

## Data Analysis

This thesis details the method of transverse energy analysis through the use of  $p_T$  spectra from the STAR BES data. As described in section 4.3.3, the TPCs and TOF detectors in STAR can identify particles as well as their trajectories and ultimately measure their multiplicity distributions with respect to the momenta. The available distributions were extrapolated to calculate the transverse energies and charged particle multiplicities. Details follow.

### 5.1 STAR $p_T$ Spectra

Adamczyk et al. [18] reports the results for the midrapidity ( $|y| < 0.1$ )  $p_T$  spectra for six different identified hadrons,  $\pi^+$ ,  $\pi^-$ ,  $K^+$ ,  $K^-$ ,  $p$ , and  $\bar{p}$ , from the STAR experiment. The spectra come from  $\sqrt{s_{NN}} = 7.7$ , 11.5, and 39 GeV Au+Au collisions data taken in the year 2010, and from  $\sqrt{s_{NN}} = 19.6$  and 27 GeV Au+Au collisions data taken in 2011, both as part of the BES Program. Figure 5.1 [18] shows the spectra corresponding to 39 GeV collisions categorized into seven different collision centrality classes. Additionally, preliminary spectra were available from the STAR experiment for identified lambdas and anti-lambdas [62]. All of these spectra were used to calculate the total transverse energy per event per particle species. This result was then used to estimate the total transverse energy due to all the collision products. The corrections applied by Adamczyk et al. [18] to the raw data to

obtain the spectra and the reported systematic uncertainties in their results are discussed below.

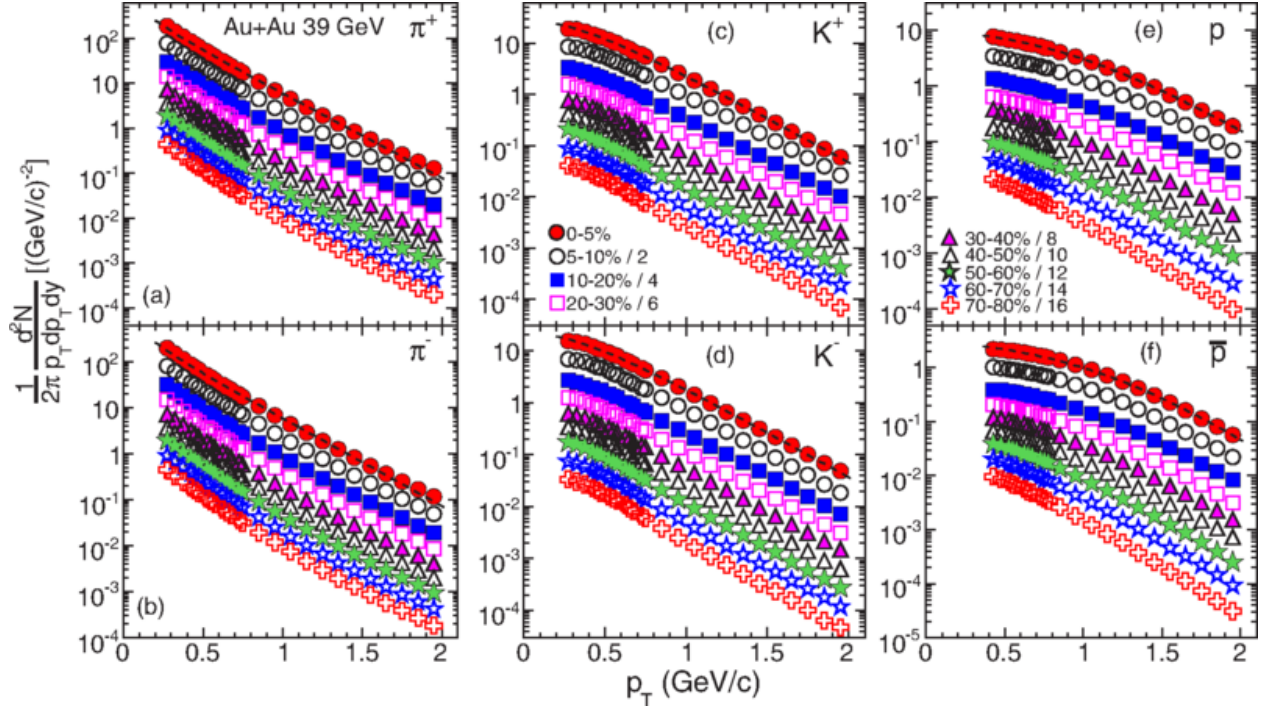


**Figure 5.1:** Transverse momentum spectra for  $\pi^+$ ,  $\pi^-$ ,  $K^+$ ,  $K^-$ ,  $p$ , and  $\bar{p}$  at midrapidity ( $|y| < 0.1$ ) from 39 GeV Au+Au collisions at RHIC. The fitting curves on the 0-5% central collision spectra for pions, kaons, and protons/anti-protons represent, respectively, the Bose-Einstein,  $m_T$ -exponential, and double-exponential functions [18].

### 5.1.1 Corrections and Systematic Uncertainties

Detector acceptance and efficiency of reconstructing particle tracks account for most of the correction applied to the raw spectra. The efficiency  $\times$  acceptance correction factor is obtained as the ratio of the distribution of the reconstructed tracks from the experiment and the tracks simulated using the GEANT model of STAR. The inverse of this factor is used to scale the raw spectra. Figure 5.2 shows typical efficiency  $\times$  acceptance factors as functions of  $p_T$  for 0-5% central 7.7 GeV collisions.

Not all tracks formed in the TPC propagate to the TOF. A correction, called the TOF matching efficiency, is applied to the spectra obtained from the TOF. This correction is defined as the ratio of the number of tracks obtained from the TOF to the total number of

619 tracks obtained from the TPC within the same acceptance. The inverse of the TOF matching  
 620 efficiency is used to scale the TOF raw yields.

621 The algorithm used by STAR for track reconstruction assumes that each particle is a pion.  
 622 A third correction is applied using a Monte Carlo simulation to account for the presence of the  
 623 proton and the kaon tracks apart from the pion tracks. Two other corrections are obtained  
 624 to subtract the backgrounds of secondary pions and protons produced from the interactions  
 625 with the detector materials and those of the pions attributable to muon contamination and  
 626 feed-down contribution from weak decays.

627 The systematic uncertainties are obtained by varying the analysis cuts and by estimating  
 628 the tracking efficiencies for each of the identified particles. The former source contributes 4%,  
 629 3%, and 6% respectively and the latter 5% each for pions, kaons, and protons. Furthermore,  
 630 the aforementioned energy loss correction contributes 3% and 5% systematic uncertainties  
 631 for kaons and protons, respectively.

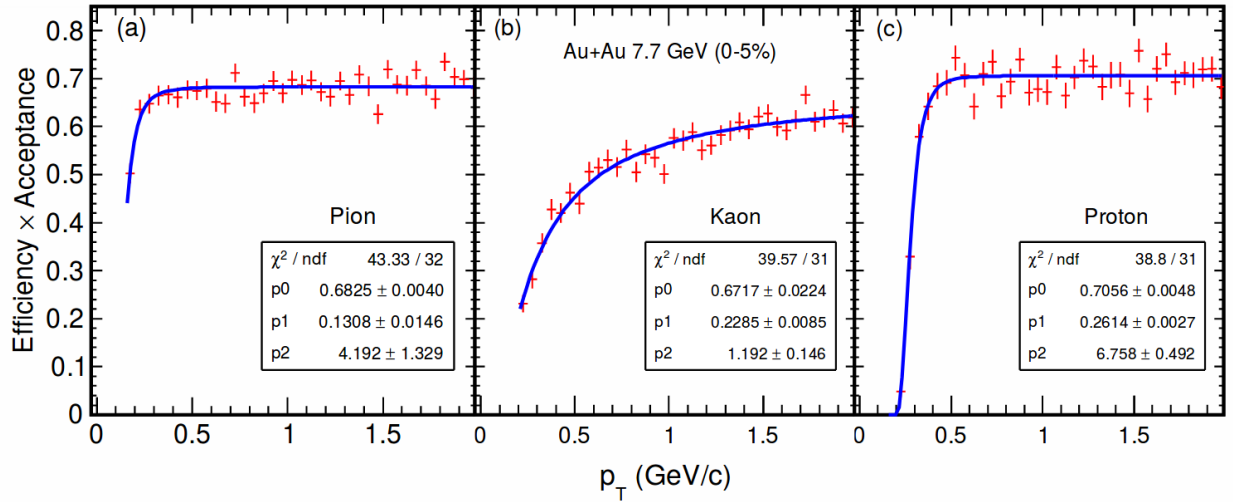


**Figure 5.2:** Midrapidity efficiency  $\times$  acceptance as a function of  $p_T$  calculated from STAR TPC Monte Carlo simulation of reconstructing (a) pions, (b) kaons, and (c) protons for 0-5% central 7.7 GeV Au+Au collisions. The curves represent functional fits of the form  $y \propto e^{-\frac{1}{x}}$  [18].

## 5.2 Extrapolation of Spectra

The available spectra were limited to a range of transverse momenta from around 0.25 GeV/c to around 2 GeV/c (for pions). At higher momenta, with model-dependent values, the  $p_T$  spectra may be dominated by hard-scattering processes. To account for the transverse energy corresponding to the momenta for which there were no available data, an extrapolation had to be used. The model used for the extrapolation and the associated statistics are discussed below.

### 5.2.1 Boltzmann-Gibbs Blast Wave

The blast wave is a common model used in the analysis of particle momentum distributions [63, 64, 18]. The specific model used in this thesis is the Boltzmann-Gibbs blast wave (BGBW). This model assumes local thermal equilibrium at the kinetic freeze-out temperature for the applicability of a Boltzmann distribution. It also assumes a radially increasing velocity that attains a maximum value at the surface of the expanding fireball [64]. The BGBW is represented by the equation:

$$\frac{dN}{dp_T} \approx \int_0^R r dr p_T m_T I_0\left(\frac{p_T \sinh \rho}{T}\right) K_1\left(\frac{m_T \cosh \rho}{T}\right), \quad (5.1)$$

where  $\rho = \tanh^{-1} \beta$  is the flow profile,  $\beta = \beta_{max}(\frac{r}{R})^n$  is the flow velocity,  $n$  is the flow velocity profile exponent,  $r$  is the radial distance from the collision vertex,  $R$  is the distance of the expanding medium surface from the collision vertex,  $m_T$  is the transverse mass given by Eq. 4.2,  $T$  is the thermal freeze-out temperature, and  $I_0(x)$  and  $K_1(x)$  ( $x$  being the placeholder for the function arguments) are the modified Bessel functions of the first and second kind.

### 5.2.2 Fitting Spectra to BGBW

Figure 5.3 presents an example of a BGBW fit on one of the individual particle spectra with  $\chi^2/\text{ndf}$  as well as other statistics and the associated uncertainties. The fitting is done in the ROOT software framework which is widely used in high energy physics data analysis.  $T$ ,  $\beta$ ,



and  $n$  are treated as free parameters, while  $m$  is fixed. The results of the fits for each of the spectra are tabulated in appendix B

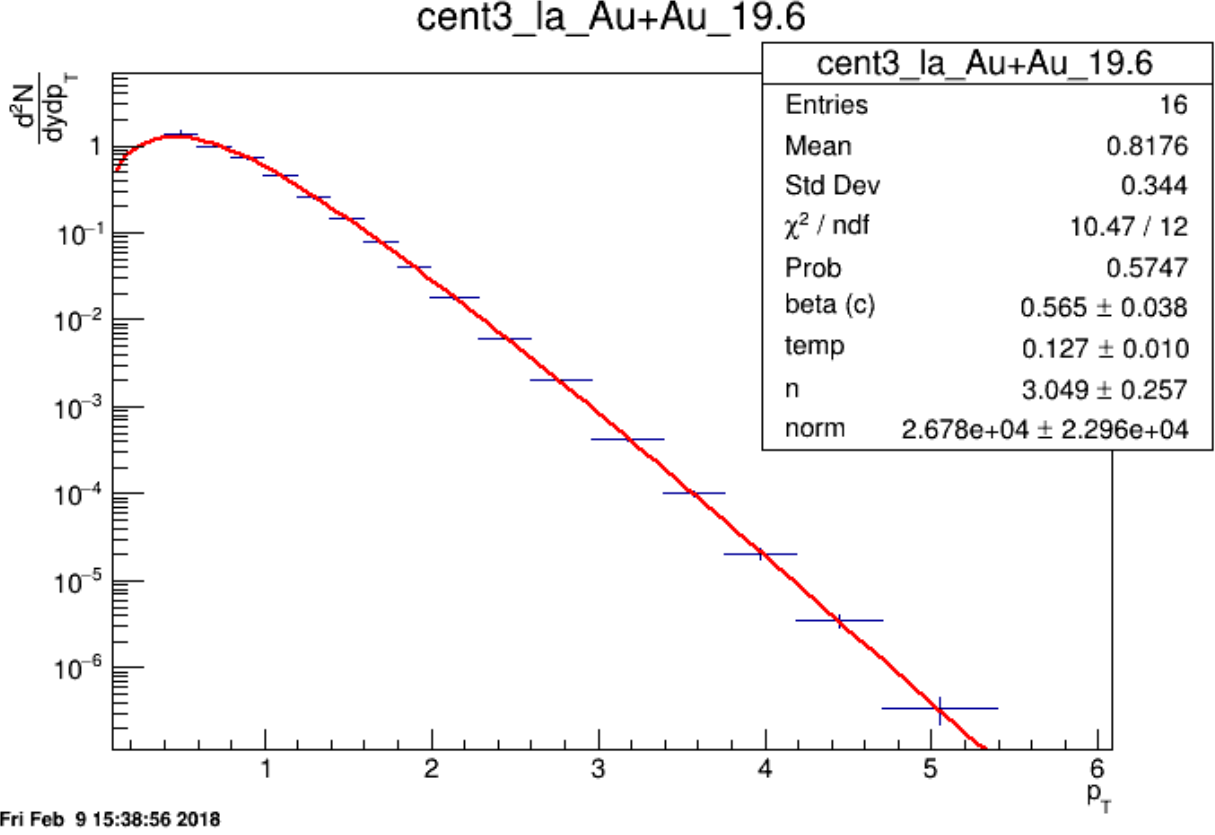


**Figure 5.3:** Red curve shows the Boltzmann-Gibbs blast wave functional fit on the preliminary transverse momentum spectrum for lambda particles identified by the STAR detector for 19.6 GeV Au+Au collisions (10-15% central). Parameters extracted from the chi-square goodness-of-fit test, as well as other statistics, are shown in the box on the top right.

## 5.3 Calculations from the Spectra

### 5.3.1 Calculation of $\frac{dE_T}{dy}$ , $\frac{dE_T}{d\eta}$ , $\frac{dN_{ch}}{dy}$ , and $\frac{dN_{ch}}{d\eta}$

The available multiplicity distribution for the  $p_T$  range,  $p_{T,low}$  to  $p_{T,high}$ , of a spectrum divided the total spectrum into three different regions: (i) region where the experimental data is available, i.e.,  $p_{T,low}$  to  $p_{T,high}$ , (ii) extrapolation region from  $p_T = 0$  GeV/c to  $p_T = p_{T,low}$ , and (iii) extrapolation region from  $p_T = p_{T,high}$  to  $p_T = 10$  GeV/c. Following the

663 methods and the Jacobian transformation described in section 4.3.2,  $\frac{dE_T}{dy}$ ,  $\frac{dE_T}{d\eta}$ ,  $\frac{dN_{ch}}{dy}$ , and  $\frac{dN_{ch}}{d\eta}$   
664 the spectra were calculated by adding said quantities corresponding to the three different  
665 regions in the distribution.

### 666 5.3.2 Assumptions, Estimation of Total $E_T$ , and Uncertainties

667 It is assumed that most of the  $E_T$  is attributable to the contributions from pions, kaons,  
668 protons and neutrons. Contributions from heavier particles are assumed to be negligible,  
669 and there are some particles which are light but decay very rapidly into  $\pi/K/p$  which are  
670 included in the spectra. It is also reasonable to assume that, at high energies, there should  
671 be roughly the same multiplicity of all the isospin states and anti-particles of a final state  
672 particle. This assumption was partially tested by comparing the  $E_T$  values calculated for the  
673 identified charged particles with those independently calculated for their anti-particles for  
674 the same values of collision energy and centrality. The comparisons revealed the  $E_T$  values  
675 of the particles being almost exactly equal to those of the anti-particles. This assumption  
676 is used to account for the energies of the isospin states of the pions, kaons and protons that  
677 were not identified.

678 Table 5.1 lists the isospin states and the anti-particles associated with the pion, the kaon,  
the proton, and the lambda particles.

Particle	Isospin multiplets
pion	$\pi^+, \pi^0, \pi^-$
kaon	$K^+, K^0, K^-, \bar{K}^0$
proton	$p, n, \bar{p}, \bar{n}$
lambda	$\Lambda, \bar{\Lambda}$

**Table 5.1:** Isospin states of different identified particles.

679

680 The total  $E_T$  for all the particles would then be:

$$E_T = \frac{3}{2}(E_T^{\pi^+} + E_T^{\pi^-}) + 2(E_T^{K^+} + E_T^{K^-}) + 2(E_T^p + E_T^{\bar{p}}) + E_T^\Lambda + E_T^{\bar{\Lambda}} \quad (5.2)$$

681 There are three major sources of systematic uncertainties: (i) uncertainties in the spectra  
682 available from [18], (ii) assumptions involved in the fitting function which mainly affects the

683 extrapolation toward lower  $p_T$  values, and (iii) assumption regarding particle ratios and that  
 684 most of the  $E_T$  is only carried by the particles listed in table 5.1. Uncertainties from the  
 685 first source are propagated in the parameter uncertainties in the best-fit function, which  
 686 are then propagated using the covariance matrices of the parameters to the  $E_T$  and  $N_{ch}$   
 687 results. Statistical uncertainties in the available data, which were small as compared to  
 688 the corresponding systematic uncertainties, were added to the systematic uncertainties in  
 689 quadrature. Uncertainties from the second source can be calculated by using several models,  
 690 apart from the BGBW, to perform the extrapolations. Each of the models would have  
 691 different assumptions involved in it, and the variation in the  $E_T$  results from the different  
 692 models can give an estimate of the systematic uncertainties arising from the difference in  
 693 the assumptions. Due to the time constraint for the completion of this thesis, calculation  
 694 of these uncertainties are left for future work. Uncertainties from the third source result  
 695 from the assumption of the calculation and would not be quantified. The uncertainties are  
 696 assumed to be 100% correlated point to point, and uncorrelated between different particles.

### 697 **5.3.3 Lambdas Centrality Adjustments and $E_T$ Interpolations**

698 The centrality bins corresponding to the lambdas spectra were slightly different from those  
 699 corresponding to the rest of the particles. The centralities were binned the same way from 0%  
 700 to 40%. However, the peripheral centralities for the lambdas were binned into 40-60% and  
 701 60-80% bins, whereas, for the rest of the particles, the peripheral centralities were binned into  
 702 40-50%, 50-60%, 60-70%, and 70-80% bins. For consistency, the lambdas  $E_T$  calculations  
 703 were interpolated to the centralities corresponding to  $\pi/K/p$  using the *Eval()* method of the  
 704 *TGraph* class in the ROOT framework.

# Chapter 6

## Results

The results of the analysis are shown in Figs. 6.1-6.9. The error bars in the figures represent the uncertainties propagated from the available data as explained in section 5.3.2. In the plots with  $\sqrt{s_{NN}}$  as the abscissa, error bars are drawn only on the distribution corresponding to 0-5% central collision for clarity.

Figure 6.1 shows how the transverse energy per nucleon participant pair scales with the total number of nucleon participants in the collisions. As discussed in section 3.2,  $N_{part}$  is generally proportional to the centrality. The results show that the normalized  $E_T$  does not vary much with  $N_{part}$  for more central collisions (higher  $N_{part}$  values). At a comprehensive stance, this quantity tends to increase with increasing  $N_{part}$ . It is also seen that the shape of the distribution of this quantity as a function of  $N_{part}$  stays roughly the same for different collision energies. Furthermore, the normalized  $E_T$  is found to increase with the collision energy, mostly when the number of participants is high. Figure 6.2 is similar to Fig. 6.1 but in rapidity instead of pseudorapidity coordinates. It shows a similar trend, but with an upward shift, of  $E_T$  distributions.

Figure 6.3 shows the dependence of  $E_T/N_{ch}$  on the number of nucleon participants. This ratio carries information about the average transverse mass of the final state particles produced from heavy ion collisions, and it has been found to not vary with the collision energy and centrality at RHIC energies [19]. The results of this analysis show that this ratio remains roughly the same at higher values of  $N_{part}$  but tends to grow smaller with decreasing  $N_{part}$ , albeit within the error bounds. It is also seen to increase with increasing

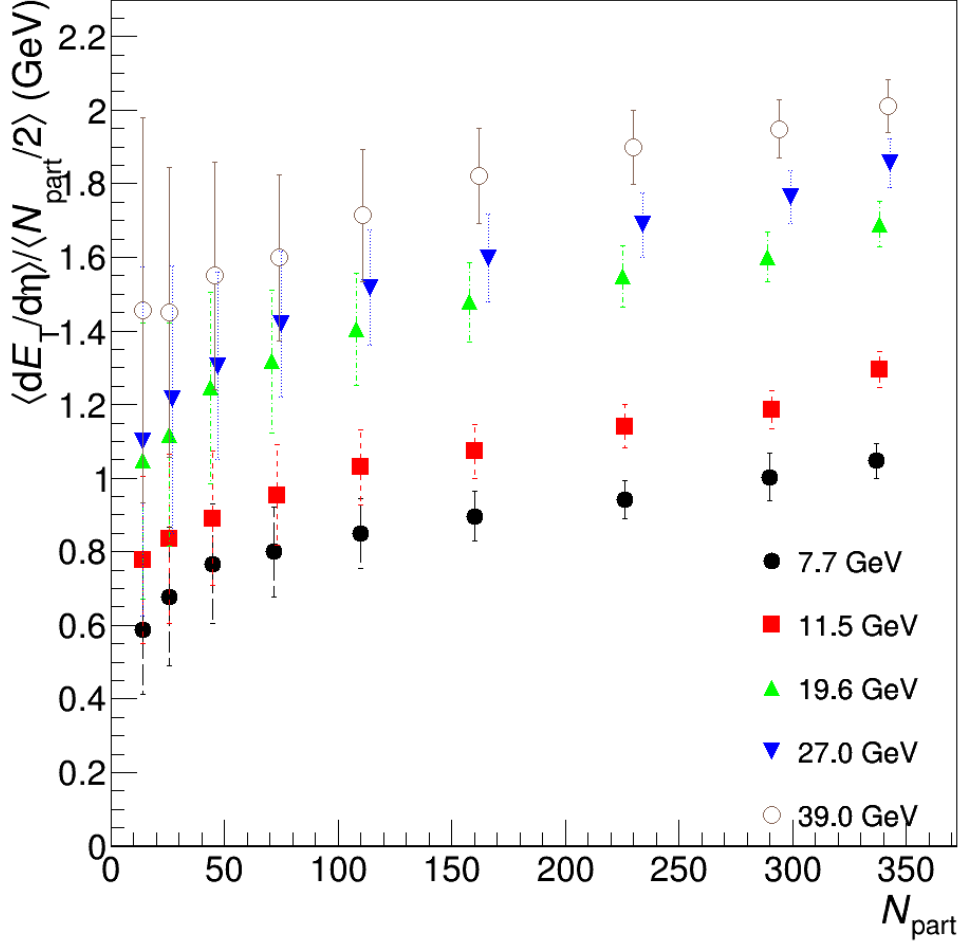
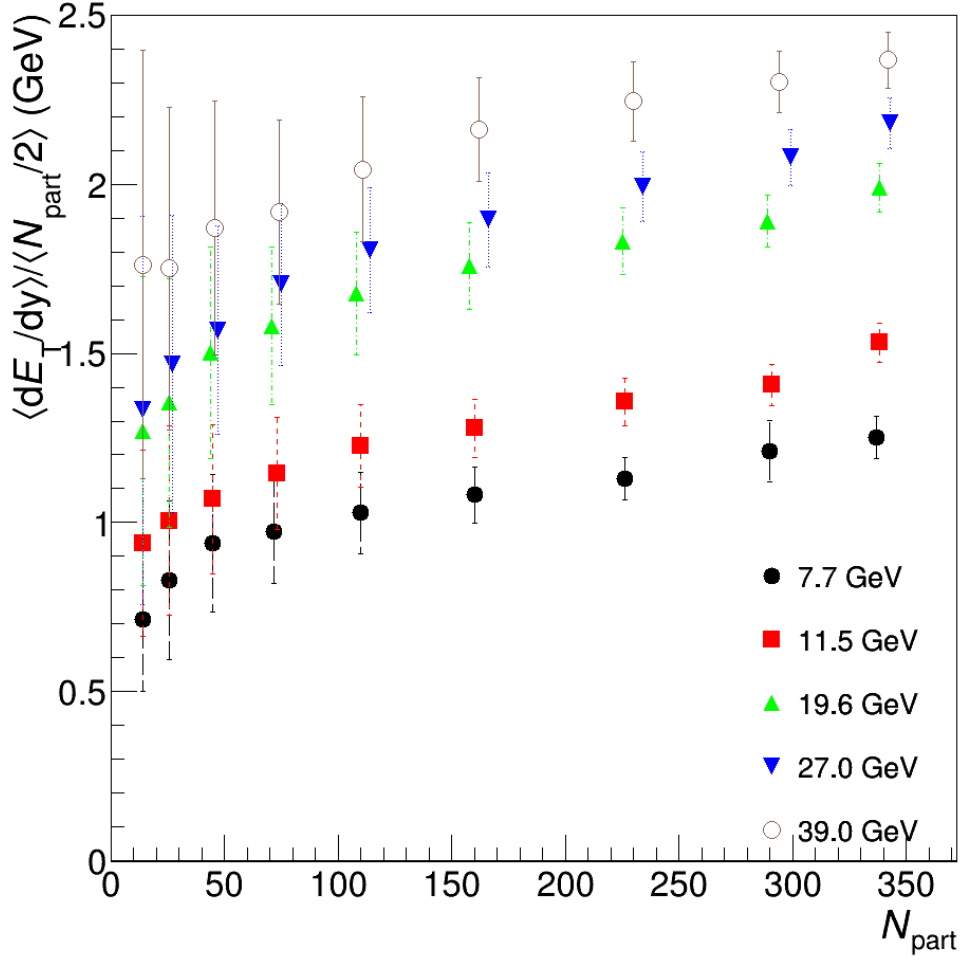


**Figure 6.1:**  $(dE_T/d\eta)/0.5N_{part}$  at midrapidity as a function of  $N_{part}$  for different collision energies.

collision energy. Figure 6.4 is similar to Fig. 6.3 but in rapidity instead of pseudorapidity coordinates. The distributions show a similar trend although with some upward shift.

Figure 6.5 shows the normalized  $E_T$  as a function of collision energy for all the different collision centralities. This quantity increases with increasing collision energy and centrality while staying within the error bounds of the closest neighboring centralities. The slope of the distribution does not seem to vary a lot between centralities. Figure 6.6 is similar to Fig. 6.5 but in rapidity instead of pseudorapidity coordinates.

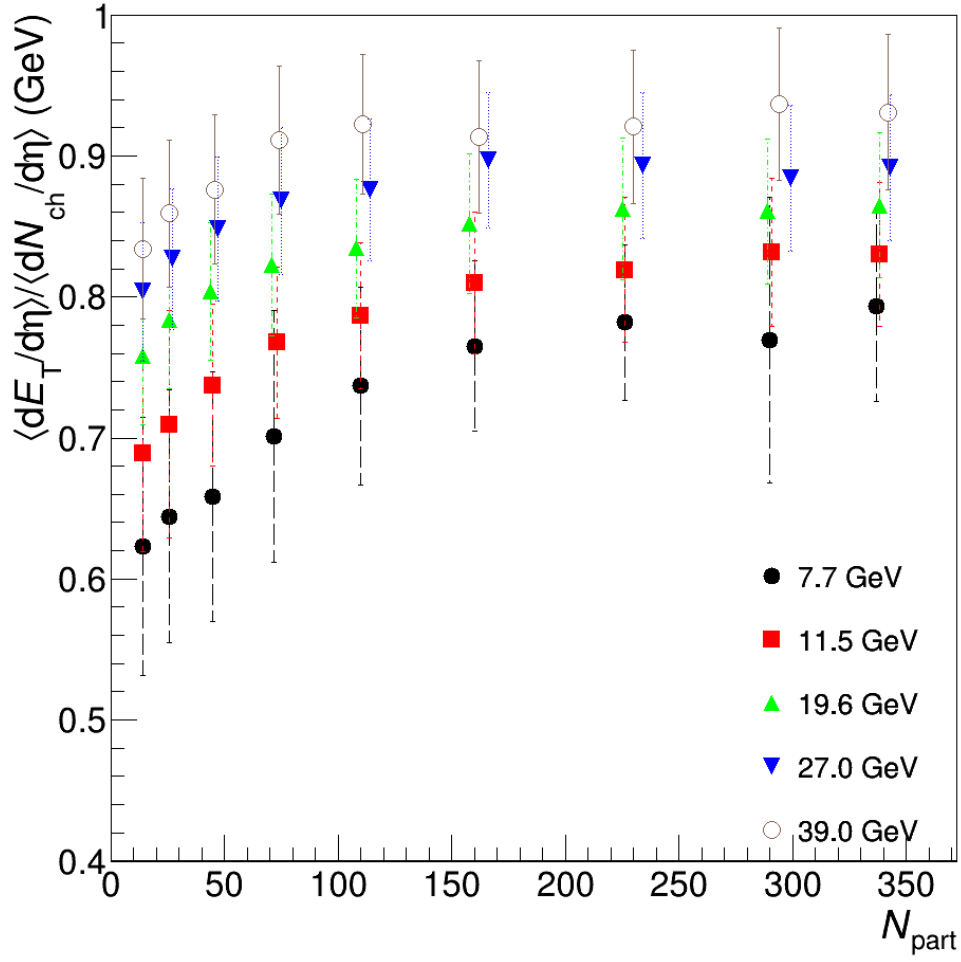
Figures 6.7 and 6.8 show the dependence of  $E_T/N_{ch}$  on the collision energy in, respectively, pseudorapidity and rapidity coordinates. The  $\sqrt{s_{NN}}$  axis is again in logarithmic scale. The



**Figure 6.2:**  $\langle dE_T/dy \rangle / 0.5N_{part}$  at midrapidity as a function of  $N_{part}$  for different collision energies.

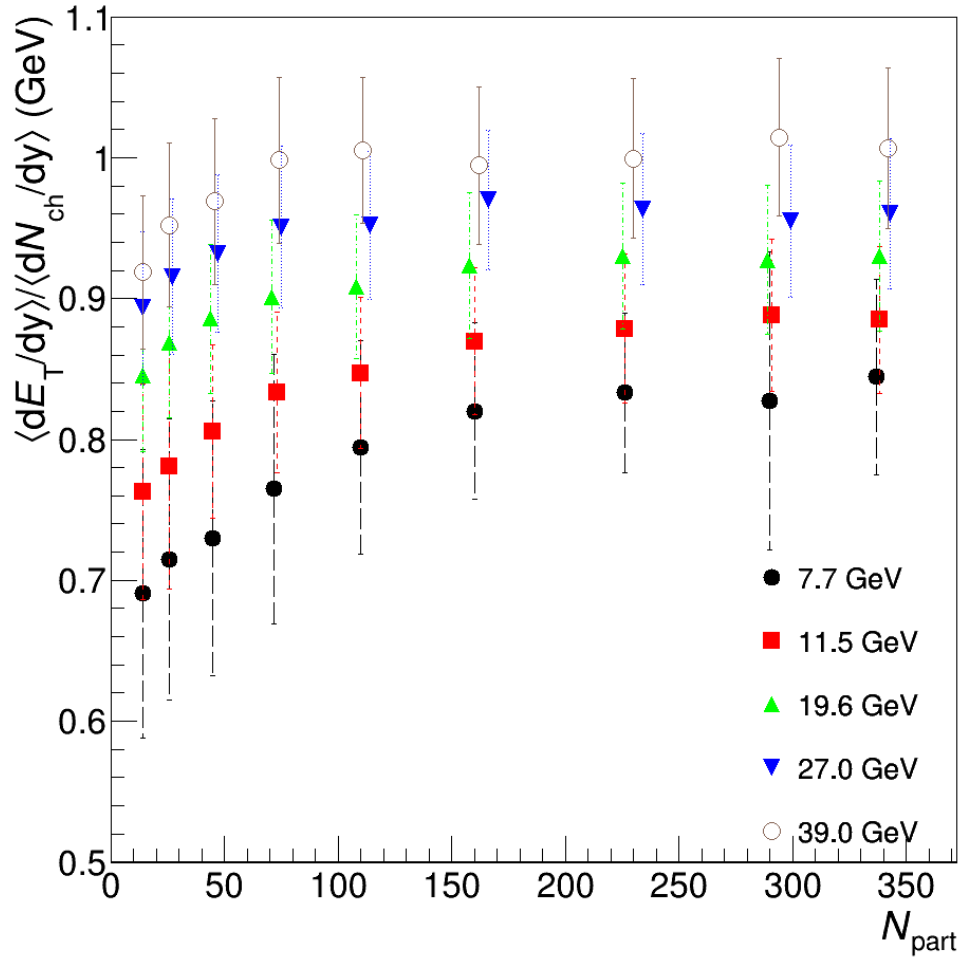
ratio  $E_T/N_{ch}$  increases with increasing collision energy. The slope of the distributions seem to decrease with increasing centrality for the more central collisions. The more central collisions also show fluctuations in the way  $E_T/N_{ch}$  increases as a function of  $\sqrt{s_{NN}}$ .

Figure 6.9 puts the 0-5% collision results of this analysis in perspective with the result from [19] based on PHENIX calorimetry. The normalized  $E_T$  from this analysis is higher than that from PHENIX for all the available collision energies. The  $\langle dE_T/dy \rangle / 0.5N_{part}$  values for  $\sqrt{s_{NN}} = 7.7, 19.6, 27$ , and 39 GeV are found to differ by 2.82, 2.83, 2.37 and 1.67 standard deviations respectively. The explanation of these differences require a thorough analysis of



**Figure 6.3:**  $(dE_T/d\eta)/(dN_{ch}/d\eta)$  at midrapidity as a function of  $N_{part}$  for different collision energies.

the assumptions made by both measurements and is not completed in this thesis due to time constraints.



**Figure 6.4:**  $(dE_T/dy)/(dN_{ch}/dy)$  at midrapidity as a function of  $N_{part}$  for different collision energies.



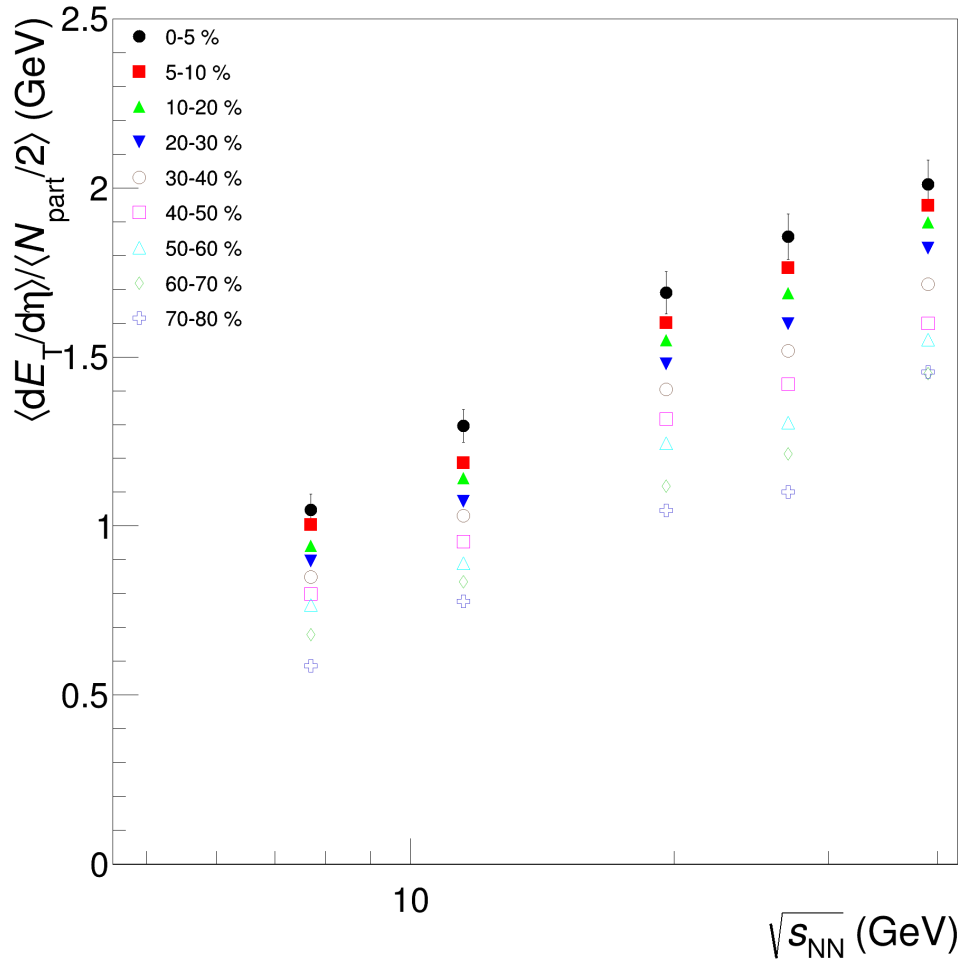


**Figure 6.5:**  $(dE_T/d\eta)/0.5N_{part}$  at midrapidity as a function of  $\sqrt{s_{NN}}$  in logarithmic scale for different centralities.

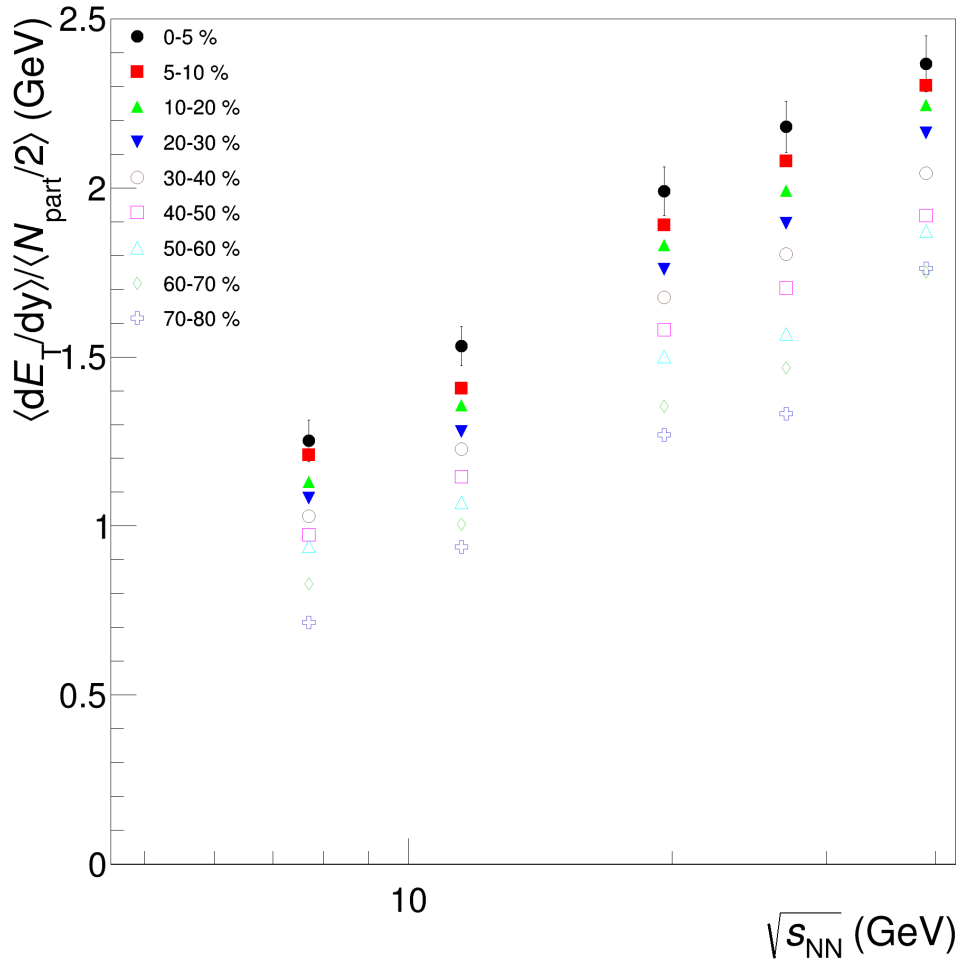


**Figure 6.6:**  $(dE_T/dy)/0.5N_{part}$  at midrapidity as a function of  $\sqrt{s_{NN}}$  for different centralities.

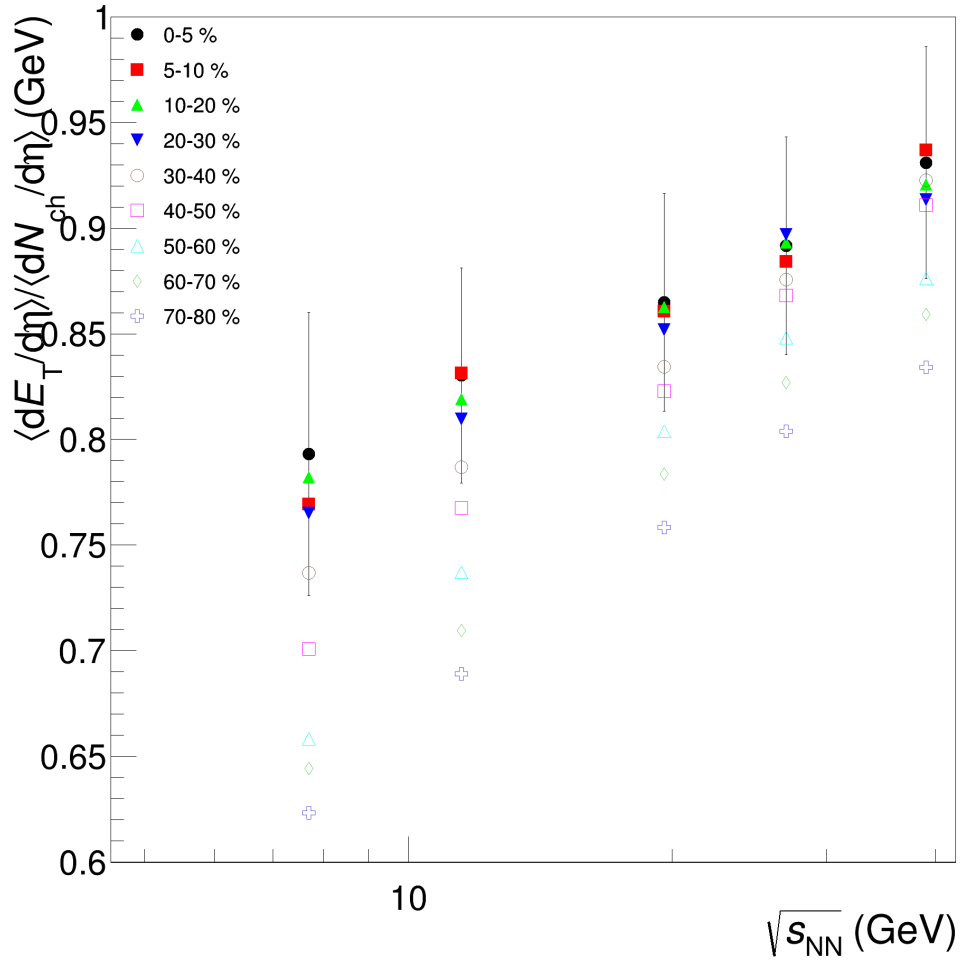


**Figure 6.7:**  $(dE_T/d\eta)/(dN_{ch}/d\eta)$  at midrapidity as a function of  $\sqrt{s_{NN}}$  for different centralities.

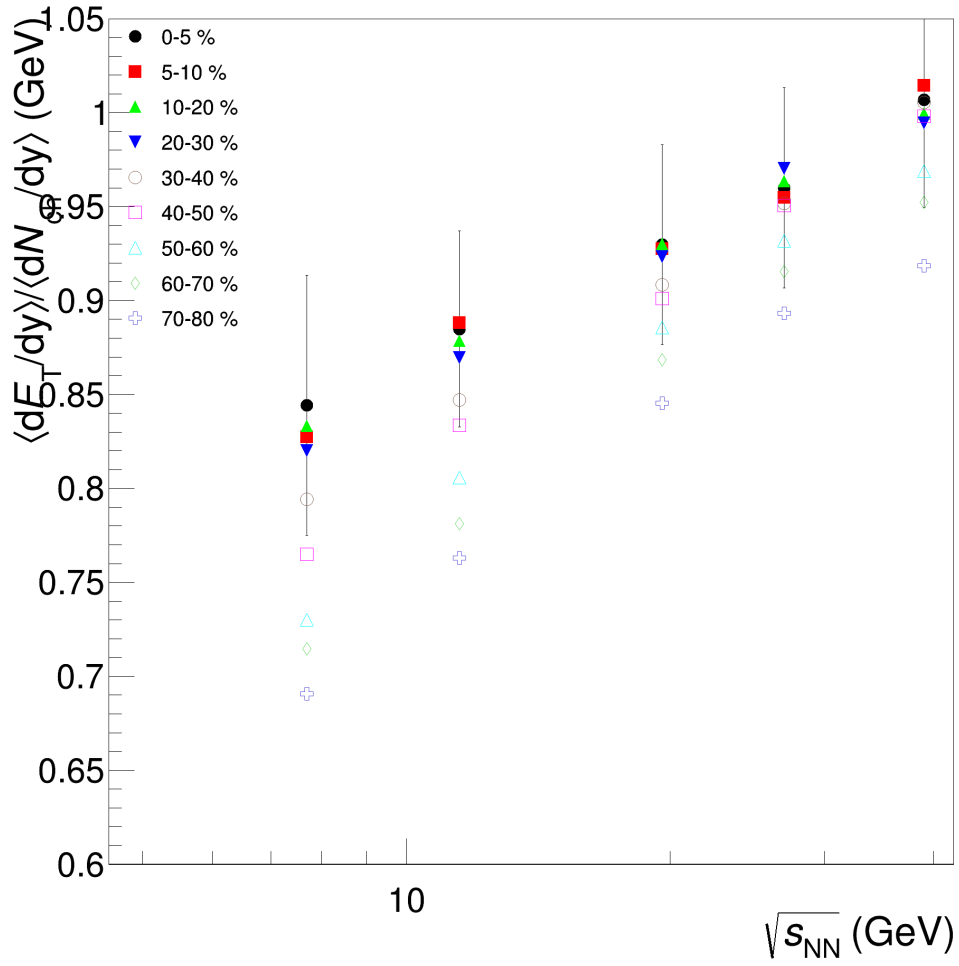


**Figure 6.8:**  $(dE_T/dy)/(dN_{ch}/dy)$  at midrapidity as a function of  $\sqrt{s_{NN}}$  for different centralities.

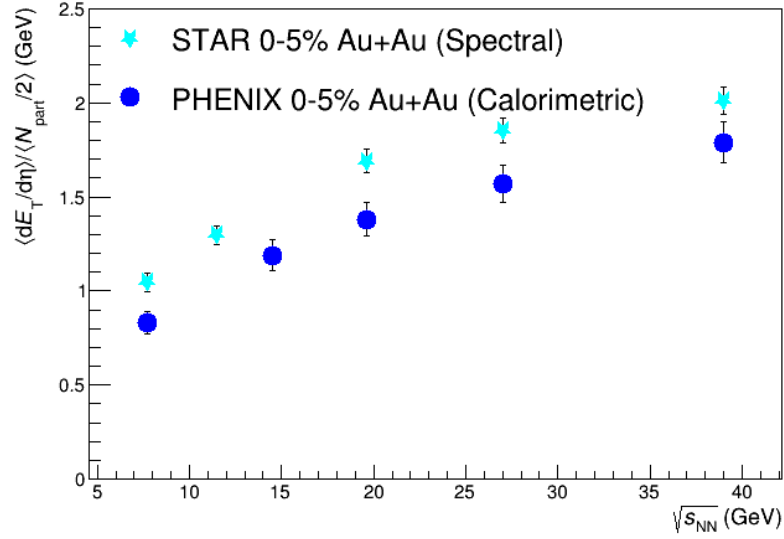


**Figure 6.9:**  $\frac{dE_T}{d\eta} / 0.5N_{part}$  for 0-5% central collisions at midrapidity as a function of  $\sqrt{s_{NN}}$ . The PHENIX data are from [19]. The error bars represent the total statistical and systematic uncertainties.

## Chapter 7

## Conclusion and Future Work

I calculated the transverse energy from Au+Au collisions at  $\sqrt{s_{NN}} = 7.7, 11.5, 19.6, 27,$  and 39 GeV for nine different centralities using the transverse momentum spectra available for identified pions, kaons and protons (and their anti-particles) and also the preliminary transverse momentum spectra available for lambdas and anti-lambdas. The Boltzmann-Gibbs Blast Wave model was used to extrapolate the spectra in the  $p_T$  regions where data were not available. I calculated the total  $E_T$  from these spectra by assuming that the contributions from heavier particles are negligible and that the different isospin states of a particle carry roughly the same amount of  $E_T$  in the aftermath of a relativistic heavy ion collision. My results show that the shapes of the distributions of  $E_T$  found from the analysis using the tracking detectors in the STAR experiment are similar to those found from the results from the electromagnetic calorimeters in the PHENIX experiment. However, the values I calculate for  $(dE_T/d\eta)/0.5N_{part}$  differ from the corresponding PHENIX calculations by 1.67 to 2.83 standard deviations at different collision energies. This discrepancy needs to be explained in the future before the codes I developed for this analysis is used for other similar analyses.

There are other aspects of this analysis that can be improved in the future. For instance, a maximum likelihood fit method can be adopted to compare the results with those using the chi-squared fits in the extrapolation of the spectra. Apart from the transverse energy, the calculation of the initial energy density,  $\epsilon$ , as given by the Bjorken formula in eq. 3.2, is possible with some more effort. It requires the estimate of other physical quantities. Adare

et al.[19] use the Glauber model to determine  $A_T$ , the area of the intersection of the two nuclei in the transverse plane. Since the results in this thesis are cross-checked with those in [19], it would be reasonable to use the same model in the future work pertaining to this thesis.

Finally, the codes in the repository can be used to analyze the data pertaining to other different collision systems. Since there is more data available on collisions of asymmetric systems such as d+Au, we can expect it to be a test to tell if the assumptions used in this analysis are reasonable for such systems. More importantly, this technique can be used to analyze higher energy RHIC data to find out if STAR spectral  $E_T$  agrees better with PHENIX calorimetric  $E_T$  when more energy is available at the time of collision.

# Bibliography



- 779 [1] C. Nattrass (2009). vi, 10, 26
- 780 [2] A. Ayala, Journal of Physics: Conference Series **761**, 012066 (2016), URL [http://](http://stacks.iop.org/1742-6596/761/i=1/a=012066)  
781 [stacks.iop.org/1742-6596/761/i=1/a=012066](http://stacks.iop.org/1742-6596/761/i=1/a=012066). vii, 5, 6
- 782 [3] S. Ozaki and T. Roser, Progress of Theoretical and Experimental Physics **2015**,  
783 03A102 (2015), [/oup/backfile/content\\_public/journal/ptep/2015/3/10.1093\\_](http://oup/backfile/content_public/journal/ptep/2015/3/10.1093_ptep_ptu093/4/ptu093.pdf)  
784 [ptep\\_ptu093/4/ptu093.pdf](http://oup/backfile/content_public/journal/ptep/2015/3/10.1093_ptep_ptu093/4/ptu093.pdf), URL [+http://dx.doi.org/10.1093/ptep/ptu093](http://dx.doi.org/10.1093/ptep/ptu093). vii,  
785 8
- 786 [4] M. Connors, C. Nattrass, R. Reed, and S. Salur (2017), 1705.01974. vii, 10, 11, 13
- 787 [5] V. Vovchenko, D. Anchishkin, and L. P. Csernai, Phys. Rev. C **90**, 044907 (2014), URL  
788 <https://link.aps.org/doi/10.1103/PhysRevC.90.044907>. vii, 12
- 789 [6] A. Adare, S. Afanasiev, C. Aidala, N. N. Ajitanand, Y. Akiba, H. Al-Bataineh,  
790 J. Alexander, A. Al-Jamel, K. Aoki, L. Aphecetche, et al., Physical Review Letters  
791 **98**, 162301 (2007), [nucl-ex/0608033](https://arxiv.org/abs/nuc1-ex/0608033). vii, 15, 16
- 792 [7] C.-Y. Wong, *Introduction to high-energy heavy-ion collisions* (World scientific, 1994).  
793 vii, 16, 17, 55
- 794 [8] H. Stcker, Nuclear Physics A **750**, 121 (2005), ISSN 0375-9474, quark-Gluon Plasma.  
795 New Discoveries at RHIC: Case for the Strongly Interacting Quark-Gluon Plasma.  
796 Contributions from the RBRC Workshop held May 14-15, 2004, URL [http://www.](http://www.sciencedirect.com/science/article/pii/S0375947404013028)  
797 [sciencedirect.com/science/article/pii/S0375947404013028](http://www.sciencedirect.com/science/article/pii/S0375947404013028). viii, 18
- 798 [9] S. Afanasiev et al. (PHENIX), Phys. Rev. Lett. **109**, 152302 (2012). viii, 19
- 799 [10] A. Adare et al. (PHENIX), Phys. Rev. Lett. **101**, 232301 (2008). viii, 19
- 800 [11] A. Adare et al. (PHENIX), Phys. Rev. **C82**, 011902 (2010). viii, 19
- 801 [12] A. Adare et al. (PHENIX), Phys. Rev. **C93**, 024904 (2016). viii, 19
- 802 [13] A. Adare et al. (PHENIX), Phys. Rev. **C88**, 024906 (2013). viii, 19

- [14] A. Adare et al. (PHENIX), Phys. Rev. Lett. **98**, 232301 (2007). viii, 19
- [15] A. Adare et al. (PHENIX), Phys. Rev. **C84**, 044902 (2011). viii, 19
- [16] A. Adare et al. (PHENIX Collaboration), Phys.Rev. **C84**, 044905 (2011). viii, 19
- [17] M. Anderson et al., Nucl. Instrum. Meth. **A499**, 659 (2003), nucl-ex/0301015. viii, 26, 27
- [18] L. Adamczyk, J. K. Adkins, G. Agakishiev, M. M. Aggarwal, Z. Ahammed, N. N. Ajitanand, I. Alekseev, D. M. Anderson, R. Aoyama, A. Aparin, et al. (STAR Collaboration), Phys. Rev. C **96**, 044904 (2017), URL <https://link.aps.org/doi/10.1103/PhysRevC.96.044904>. viii, 24, 28, 29, 30, 31, 33
- [19] A. Adare, S. Afanasiev, C. Aidala, N. N. Ajitanand, Y. Akiba, R. Akimoto, H. Al-Bataineh, J. Alexander, M. Alfred, A. Al-Jamel, et al. (PHENIX Collaboration), Phys. Rev. C **93**, 024901 (2016), URL <https://link.aps.org/doi/10.1103/PhysRevC.93.024901>. ix, 5, 23, 24, 35, 37, 44, 46
- [20] D. Scott, Can. J. Phys. **84**, 419 (2006), astro-ph/0510731. 1
- [21] S. Perlmutter et al. (Supernova Cosmology Project), Astrophys. J. **517**, 565 (1999), astro-ph/9812133. 1
- [22] P. Foka and M. A. Janik, Reviews in Physics **1**, 154 (2016), ISSN 2405-4283, URL <http://www.sciencedirect.com/science/article/pii/S2405428316300156>. 1, 10
- [23] M. Gyulassy, in *Structure and dynamics of elementary matter. Proceedings, NATO Advanced Study Institute, Camyuva-Kemer, Turkey, September 22-October 2, 2003* (2004), pp. 159–182, nucl-th/0403032. 1, 7
- [24] J. Adams, M. Aggarwal, Z. Ahammed, J. Amonett, B. Anderson, D. Arkhipkin, G. Averichev, S. Badyal, Y. Bai, J. Balewski, et al., Nuclear Physics A **757**, 102 (2005), ISSN 0375-9474, first Three Years of Operation of RHIC, URL <http://www.sciencedirect.com/science/article/pii/S0375947405005294>. 1

- [25] C. L. Bennett, D. Larson, J. L. Weiland, N. Jarosik, G. Hinshaw, N. Odegard, K. M. Smith, R. S. Hill, B. Gold, M. Halpern, et al., **208**, 20 (2013), 1212.5225. 1
- [26] Planck Collaboration, P. A. R. Ade, N. Aghanim, M. Arnaud, M. Ashdown, J. Aumont, C. Baccigalupi, A. J. Banday, R. B. Barreiro, J. G. Bartlett, et al., **594**, A13 (2016), 1502.01589. 1
- [27] J. I. Kapusta, Nuclear Physics B **148**, 461 (1979), ISSN 0550-3213, URL <http://www.sciencedirect.com/science/article/pii/0550321379901469>. 3
- [28] E. V. Shuryak, Zeitschrift für Physik C Particles and Fields **38**, 141 (1988), ISSN 1431-5858, URL <https://doi.org/10.1007/BF01574528>. 3
- [29] I. Aitchison and A. Hey, *Gauge Theories in Particle Physics, Volume II: QCD and the Electroweak Theory, Third Edition*, Graduate Student Series in Physics (CRC Press, 2003), ISBN 9780849387760, URL <https://books.google.com/books?id=-mDjFSUDQsEC>. 3
- [30] G. S. Bali, Phys. Rept. **343**, 1 (2001), hep-ph/0001312. 4
- [31] H. Satz, Journal of Physics G: Nuclear and Particle Physics **32**, R25 (2006), URL <http://stacks.iop.org/0954-3899/32/i=3/a=R01>. 4, 5
- [32] J. M. Heuser, Nuclear Physics A **904-905**, 941c (2013), ISSN 0375-9474, the Quark Matter 2012, URL <http://www.sciencedirect.com/science/article/pii/S0375947413002960>. 5
- [33] J. Adam, D. Adamova, M. M. Aggarwal, G. Aglieri Rinella, M. Agnello, N. Agrawal, Z. Ahammed, S. Ahmad, S. U. Ahn, S. Aiola, et al. (ALICE Collaboration), Phys. Rev. C **94**, 034903. 30 p (2016), 30 pages, 14 captioned figures, 2 tables, authors from page 25, published version, figures at <http://aliceinfo.cern.ch/ArtSubmission/node/2400>, URL <https://cds.cern.ch/record/2139456>. 6, 14
- [34] M. Floris, Nuclear Physics A **931**, 103 (2014), ISSN 0375-9474, qUARK MATTER 2014, URL <http://www.sciencedirect.com/science/article/pii/S0375947414003716>. 6

- [35] S. Chatrchyan, V. Khachatryan, A. M. Sirunyan, A. Tumasyan, W. Adam, T. Bergauer,  
M. Dragicevic, J. Erö, C. Fabjan, M. Friedl, et al. (CMS Collaboration), Phys. Rev.  
Lett. **109**, 152303 (2012), URL [https://link.aps.org/doi/10.1103/PhysRevLett.](https://link.aps.org/doi/10.1103/PhysRevLett.109.152303)  
**109.152303**. 6, 21
- [36] R. Stock, J. Phys. **G30**, S633 (2004), [nuc1-ex/0405007](https://arxiv.org/abs/nuc1-ex/0405007). 7
- [37] L. Evans and P. Bryant, Journal of Instrumentation **3**, S08001 (2008), URL <http://stacks.iop.org/1748-0221/3/i=08/a=S08001>. 9
- [38] C. Loizides, J. Nagle, and P. Steinberg, SoftwareX **1-2**, 13 (2015), [1408.2549](https://arxiv.org/abs/1408.2549). 10
- [39] M. L. Miller, K. Reygers, S. J. Sanders, and P. Steinberg, Ann. Rev. Nucl. Part. Sci.  
**57**, 205 (2007), [nuc1-ex/0701025](https://arxiv.org/abs/nuc1-ex/0701025). 10
- [40] J. D. Bjorken, Phys. Rev. D **27**, 140 (1983), URL [https://link.aps.org/doi/10.](https://link.aps.org/doi/10.1103/PhysRevD.27.140)  
**1103/PhysRevD.27.140**. 13
- [41] P. Jacobs and X.-N. Wang, Progress in Particle and Nuclear Physics **54**, 443 (2005),  
[hep-ph/0405125](https://arxiv.org/abs/hep-ph/0405125). 14
- [42] B. Schenke, Nuclear Physics A **967**, 105 (2017), ISSN 0375-9474, the 26th International  
Conference on Ultra-relativistic Nucleus-Nucleus Collisions: Quark Matter 2017, URL  
<http://www.sciencedirect.com/science/article/pii/S0375947417301343>. 14
- [43] M. Strickland, Nuclear Physics A **926**, 92 (2014), [1401.1188](https://arxiv.org/abs/1401.1188). 14
- [44] P. Huovinen, P. F. Kolb, U. Heinz, P. V. Ruuskanen, and S. A. Voloshin, Physics Letters  
B **503**, 58 (2001), [hep-ph/0101136](https://arxiv.org/abs/hep-ph/0101136). 14
- [45] R. Snellings, New Journal of Physics **13**, 055008 (2011), [1102.3010](https://arxiv.org/abs/1102.3010). 14
- [46] J.-F. Paquet, C. Shen, G. Denicol, M. Luzum, B. Schenke, S. Jeon, and C. Gale, Nuclear  
Physics A **956**, 409 (2016), ISSN 0375-9474, the XXV International Conference on  
Ultrarelativistic Nucleus-Nucleus Collisions: Quark Matter 2015, URL [http://www.](http://www.sciencedirect.com/science/article/pii/S0375947416000828)  
[sciencedirect.com/science/article/pii/S0375947416000828](http://www.sciencedirect.com/science/article/pii/S0375947416000828). 15, 16

- [47] M. Wilde (ALICE), Nucl. Phys. **A904-905**, 573c (2013), 1210.5958. 16
- [48] D. Elia and the ALICE Collaboration, Journal of Physics: Conference Series **455**, 012005 (2013), URL <http://stacks.iop.org/1742-6596/455/i=1/a=012005>. 16
- [49] N. K. Behera, R. Sahoo, and B. K. Nandi, Adv. High Energy Phys. **2013**, 273248 (2013), 1206.6616. 16
- [50] Bratkovskaya, E.L., Moreau, P., Palmese, A., Cassing, W., Seifert, E., and Steinert, T., EPJ Web Conf. **171**, 02004 (2018), URL <https://doi.org/10.1051/epjconf/201817102004>. 17
- [51] H. Sazdjian, EPJ Web Conf. **137**, 02001 (2017), 1612.04078. 17
- [52] G. Odyniec, Journal of Physics: Conference Series **455**, 012037 (2013), URL <http://stacks.iop.org/1742-6596/455/i=1/a=012037>. 19
- [53] X. Luo, Nuclear Physics A **956**, 75 (2016), ISSN 0375-9474, the XXV International Conference on Ultrarelativistic Nucleus-Nucleus Collisions: Quark Matter 2015, URL <http://www.sciencedirect.com/science/article/pii/S0375947416300112>. 19
- [54] S. S. Adler, S. Afanasiev, C. Aidala, N. N. Ajitanand, Y. Akiba, A. Al-Jamel, J. Alexander, K. Aoki, L. Aphecetche, R. Armendariz, et al. (PHENIX Collaboration), Phys. Rev. C **89**, 044905 (2014), URL <https://link.aps.org/doi/10.1103/PhysRevC.89.044905>. 21
- [55] S. S. Adler, S. Afanasiev, C. Aidala, N. N. Ajitanand, Y. Akiba, J. Alexander, R. Amirkas, L. Aphecetche, S. H. Aronson, R. Auerbeck, et al. (PHENIX Collaboration), Phys. Rev. C **71**, 034908 (2005), URL <https://link.aps.org/doi/10.1103/PhysRevC.71.034908>. 22
- [56] C. Patrignani and P. D. Group, Chinese Physics C **40**, 100001 (2016), URL <http://stacks.iop.org/1674-1137/40/i=10/a=100001>. 22
- [57] R. Preghenella (ALICE), PoS **EPS-HEP2011**, 118 (2011), 1111.0763. 24

- 905 [58] H. A. Bethe and J. Ashkin (1953). 25
- 906 [59] T. A. Collaboration, K. Aamodt, A. A. Quintana, R. Achenbach, S. Acounis,  
 907 D. Adamov, C. Adler, M. Aggarwal, F. Agnese, G. A. Rinella, et al., Journal of  
 908 Instrumentation **3**, S08002 (2008), URL [http://stacks.iop.org/1748-0221/3/i=08/](http://stacks.iop.org/1748-0221/3/i=08/a=S08002)  
 909 [a=S08002](http://stacks.iop.org/1748-0221/3/i=08/a=S08002). 25
- 910 [60] H. J. Hilke, Reports on Progress in Physics **73**, 116201 (2010), URL <http://stacks.iop.org/0034-4885/73/i=11/a=116201>. 26
- 912 [61] M. Shao, O. Yu. Barannikova, X. Dong, Y. Fisyak, L. Ruan, P. Sorensen, and Z. Xu,  
 913 Nucl. Instrum. Meth. **A558**, 419 (2006), [nuc1-ex/0505026](https://arxiv.org/abs/nuc1-ex/0505026). 26
- 914 [62] Z. Ye, private communication. 28
- 915 [63] Z. Tang, Y. Xu, L. Ruan, G. van Buren, F. Wang, and Z. Xu, Phys. Rev. **C79**, 051901  
 916 (2009), 0812.1609. 31
- 917 [64] S. Tripathy, A. Khuntia, S. K. Tiwari, and R. Sahoo, Eur. Phys. J. **A53**, 99 (2017),  
 918 1703.02416. 31

# Appendices

## A Kinematic Variables

The description of the collision physics and the interpretation of its results are aided by the construction of variables that undergo simple transformations under a change of reference frame. Two such variables, rapidity and pseudorapidity, are described in this section.

The rapidity,  $y$ , of a particle is defined as:

$$y \equiv \frac{1}{2} \ln \frac{p_0 + p_z}{p_0 - p_z} \quad (1)$$

$$= \frac{1}{2} \ln \frac{E + p_z}{E - p_z}, \quad (2)$$

where  $p_0$  and  $p_z$  are the components of its contravariant four-momentum  $p = (p_0, p_x, p_y, p_z)$  with  $p_0 = \frac{E}{c}$ ,  $E$  being the relativistic energy of the particle and  $c$ , the speed of light, being equal to 1 in natural units.

The rapidity of a particle is used as a relativistic description of its velocity. Unlike the canonical velocity of a particle, its rapidity transforms simply additively under a Lorentz boost of the frame of reference. For example, suppose a particle has a rapidity  $y$  in the laboratory frame. Let  $y'$  denote its rapidity as measured in a frame that is Lorentz boosted with a velocity  $\beta$  in the  $z$ -direction with respect to the laboratory frame. Then the relationship between the rapidities in the two different frames is simply

$$y' = y - y_\beta \quad (3)$$

Here,

$$y_\beta = \frac{1}{2} \ln \frac{1 + \beta}{1 - \beta} \quad (4)$$

is the rapidity the particle would have in the laboratory frame if it were moving with a velocity  $\beta$  in the  $z$ -direction with respect to the laboratory frame, as can be verified from equation 1 with  $p_0 = \gamma m$  and  $p_z = \gamma \beta m$ ,  $\gamma$  being the Lorentz factor  $\frac{1}{\sqrt{1-\beta^2}}$  [7].

The convenience provided by this construct comes with a cost. As evident from equation 1, the calculation of the rapidity of a particle requires the measurement of two different



940 observables associated with it, such as the energy and the  $z$ -direction momentum. However,  
 941 experimental constraints may sometimes only facilitate the measurement of the direction of  
 942 the detected particle with respect to the beam axis. What's more convenient in such a case  
 943 is the use of another variable construct called pseudorapidity,  $\eta$ , defined as:

$$\eta \equiv -\ln \tan \frac{\theta}{2}, \quad (5)$$

944 where  $\theta$  is the angle the particle's momentum vector,  $\mathbf{p}$ , makes with the  $z$ -direction. The  
 945 above equation can also be written in terms of the momentum as:

$$\eta = \frac{1}{2} \ln \frac{|\mathbf{p}| + p_z}{|\mathbf{p}| - p_z} \quad (6)$$

946 From equations 1 and 6, it is evident that  $\eta \approx y$  when  $|\mathbf{p}| \approx p_0$ , i.e., when the momentum  
 947 is large compared to the rest mass. The transformation of the particle distribution from the  
 948  $y$ -space to the  $\eta$ -space is discussed in section 4.3.2.

## <sup>949</sup> B Results from BGBW Fits